First-principles nanocircuit model of open electromagnetic resonators

Carlo Forestiere and Giovanni Miano
Department of Electrical Engineering and Information Technology, Università degli Studi di Napoli Federico II, via Claudio 21, Napoli 80125, Italy

Andrea Alù*
Photonics Initiative, Advanced Science Research Center, City University of New York, New York, New York 10031, USA
and Physics Program, Graduate Center of the City University of New York, New York, New York 10016, USA

(Received 26 March 2024; revised 29 July 2024; accepted 1 August 2024; published 5 September 2024)

We derive from first principles a general circuit model for open, frequency dispersive electromagnetic resonators in the full-wave regime. This model extends the concepts of radiation impedance to the polarization current-density modes induced in open resonators by an arbitrary external excitation. Its physics-based elements offer physical insights into the scattering problem and enable efficient modeling of the resonance frequency and associated bandwidth for arbitrary scattering resonances, establishing a powerful platform for the design and optimization of nanophotonic circuits. Our findings offer compelling prospects for electromagnetic scattering and ultrafast nanophotonics, streamlining the analysis and design of nanoresonators with enhanced operational speeds, and outlining a physics-based model of their temporal dynamics.

DOI: 10.1103/PhysRevApplied.22.034014

I. INTRODUCTION

In the past decades, nanoscale plasmonic [1] and high-index all-dielectric Mie resonators [2] have emerged as fundamental elements to design nanophotonic systems. As the complexity of arrangements of nanoparticles grows, a modular way to describe their combined response in a circuitlike fashion is highly desirable. Along this pursuit, researchers have introduced circuit analogs of nanoresonators interacting with light [3–8], and a definition of the input impedance for nanoantennas [9,10]. While these approaches provide a powerful model for light interactions with nanoparticles at specific frequencies, they fail at fully capturing the underlying physics, such as resonance frequency dispersion and associated bandwidths. These quantities are crucial not only for providing powerful insights into how nanoparticles respond when excited by light but also for addressing emerging needs in the field of nano-optics, in the context of the temporal response of nanophotonic devices and metamaterials.

We can identify several operating scenarios of nanoresonators interacting with electromagnetic fields. In the first scenario, illustrated in Fig. 1(a), the nanoresonator consists of a metal or dielectric object with a gap region where a feed, typically a localized optical emitter, is placed. The input impedance can be defined similarly to a classical antenna [11], as long as dispersion and dissipation are correctly accounted for [12]. The nanoresonator can be tuned by placing a nanoload near the gap or feeding region [9]. An alternative scenario, depicted in Fig. 1(b), involves placing the emitter in proximity to a nanoresonator without a gap region, more similar to an antenna reflector. Also, in this case, the concept of input impedance can be introduced [10]. In both scenarios, the bandwidth can be determined using established techniques from antenna design [13]. The third scenario, shown in Fig. 1(c), is the most common in the field of nanophotonics and arises when the object interacts with an incident electromagnetic field that cannot be attributed to a localized source. In the absence of a feeding point, the input impedance cannot be defined using standard antenna engineering approaches.

In this paper, we propose a circuit model for open nanoresonators, applicable to any of the scenarios in Fig. 1 and which, unlike previous approaches [3–5,7,8], can be rigorously defined in the full-wave regime. The proposed model introduces the concept of "radiation impedance" of an open resonant mode, which does not depend on the excitation condition nor on the material dispersion, and it can be rigorously defined for each of the three scenarios illustrated in Fig. 1. As a result, the proposed model allows us to transplant several classical concepts and formulas of circuit and antenna theory to the domain of electromagnetic scattering, enabling the efficient calculation and physics-rooted modeling of the resonance frequency, dispersion, and bandwidth of any open resonant

*Contact author: aalu@gc.cuny.edu

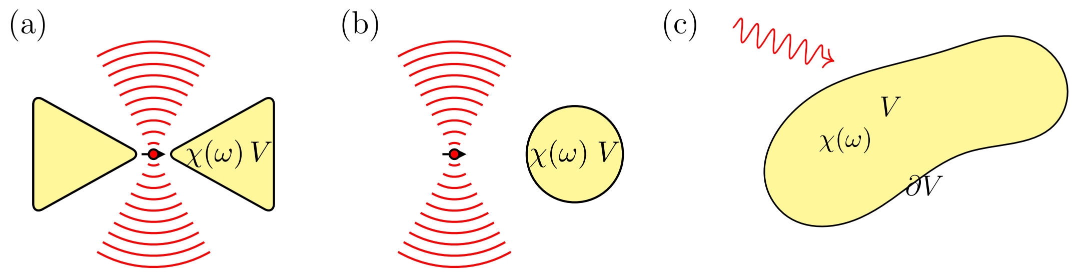

FIG. 1. Scenarios for the excitation of an electromagnetic dispersive open resonator with susceptibility $\chi(\omega)$. (a) A bow-tie nanoantenna featuring a feeding point located in its gap region. (b) A nanosphere excited by a point source, where no gap region is present. (c) A nanoresonator excited by an incident electric field coming from infinity.

electromagnetic mode. In radio-frequency and microwave engineering, tuning the input impedance to zero-reactance is critical to impedance match the antenna and ensure efficient radiation at resonance. Here, we demonstrate that the resonance condition for a resonant mode of a localized open scatterer can be determined in an analogous way by setting its reactance, as defined in our model, to zero. Furthermore, leveraging our definition of radiation impedance we can extend the Yaghjian-Best formula [13] from antenna engineering to determine the bandwidth of the open modes of a nanoresonator.

The paper is organized as follows. In Sec. II, we formulate the electromagnetic scattering problem from a homogeneous object of finite size in integral form. Here, we also introduce the modes of the nanoresonator and the definition of the radiation impedance of the modes. We then introduce the circuit model together with the definition of the constituent impedance and sources, and find the resonance condition for the modes. In Sec. III, we show how the Yaghjian-Best formula [13] can be employed to calculate the bandwidth of arbitrary open resonant modes using the introduced radiation impedance. Then, in Sec. IV, we derive the electroquasistatic and magnetoquasistatic limits of the circuit model, which are relevant for the analysis and design of plasmonic and high-permittivity resonators, respectively. In Sec. V, we apply our model to metal and dielectric nanospheres, deriving the values of the corresponding circuit elements. We then validate the calculation of the resonance frequency and bandwidth for object dimensions comparable to the incident wavelength. In Sec. VI, we conclude with a summary and a discussion of the main achievements.

II. MODE EXPANSION, CIRCUIT MODEL, AND RESONANCES

Consider a linear, homogeneous, isotropic, and dispersive dielectric object of arbitrary shape and finite size placed in vacuum, as sketched in Fig. 1. Initially, we simplify our analysis by assuming the object is composed of a single material characterized by susceptibility $\chi(\omega)$. We will extend our discussion to include objects made of multiple materials in Appendix A. The object occupies the volume V with boundary ∂V whose normal $\hat{\mathbf{n}}$ points outward. We denote by V_e the external domain. The characteristic linear dimension ℓ_c of the object is defined as the radius of the smallest sphere that surrounds it. The object is excited by an electric field $\mathbf{E}_{\text{inc}}$ that oscillates at frequency ω (a time-harmonic dependence $e^{i\omega t}$ is assumed).

Based on the material composing the object, we define a "material impedance" $Z_m(\omega)$, defined as

$$Z_m(\omega) = R_m(\omega) + iX_m(\omega) = -i\frac{\zeta_0}{\chi(\omega)}\frac{1}{\xi}, \tag{1}$$

where ε_0 and μ_0 are the vacuum permittivity and permeability, $\zeta_0 = \sqrt{\mu_0/\varepsilon_0}$ is the characteristic impedance of the vacuum, $\xi = k_0\,\ell_c$ is the size parameter of the object, $k_0 = \omega/c_0$, and $c_0 = 1/\sqrt{\varepsilon_0\mu_0}$. For reasons that will become clear in the following, we call R_m and X_m the "material resistance" and "material reactance."

We formulate the full-wave scattering problem by considering the polarization current density field $\mathbf{J}(\mathbf{r})$, induced by the incident field $\mathbf{E}_{\text{inc}}(\mathbf{r})$ in the region V occupied by the object, as the unknown. The field $\mathbf{J}$ is related to the scattered electric field $\mathbf{E}_s(\mathbf{r})$ and the incident field $\mathbf{E}_{\text{inc}}$ through the following relation:

$$\mathbf{J}(\mathbf{r}) = i\omega\varepsilon_0\chi(\omega)\left[\mathbf{E}_s(\mathbf{r}) + \mathbf{E}_{\text{inc}}(\mathbf{r})\right] \quad \text{in } V. \tag{2}$$

Both $\mathbf{E}_s$ and $\mathbf{J}$ are solenoidal in V due to the homogeneity and isotropy of the material. By expressing $\mathbf{E}_s(\mathbf{r})$ as a function of $\mathbf{J}$, we obtain the full-wave volume integral equation (e.g., Ref. [14])

$$\begin{aligned}\frac{\zeta_0}{i\xi\chi}\mathbf{J}(\mathbf{r}) = &-\frac{\zeta_0}{i\xi}\nabla_{\mathbf{r}}\oint_{\partial V}\frac{e^{-i\xi|\mathbf{r}-\mathbf{r}'|/\ell_c}}{4\pi|\mathbf{r}-\mathbf{r}'|}\mathbf{J}(\mathbf{r}')\cdot\hat{\mathbf{n}}(\mathbf{r}')\,d^2\mathbf{r}' \\ &+\frac{\zeta_0}{i}\frac{\xi}{\ell_c^2}\int_V\frac{e^{-i\xi|\mathbf{r}-\mathbf{r}'|/\ell_c}}{4\pi|\mathbf{r}-\mathbf{r}'|}\mathbf{J}(\mathbf{r}')\,d^3\mathbf{r}' \\ &+\frac{\mathbf{E}_{\text{inc}}(\mathbf{r})}{\ell_c} \quad \forall\,\mathbf{r}\in V. \end{aligned} \tag{3}$$

Here, the surface and volume integrals represent the contributions to the induced electric field due to the scalar and vector potentials in the Lorenz gauge, respectively. Equation (3) can be rewritten as [15]

$$Z_m(\omega)\,\mathbf{J}(\mathbf{r}) + \mathscr{L}\{\mathbf{J}\}(\mathbf{r}) = \frac{\mathbf{E}_{\rm inc}(\mathbf{r})}{\ell_c} \quad \forall\,\mathbf{r}\in V, \tag{4}$$

where $Z_m(\omega)$ is the material impedance defined in Eq. (1), and the operator $\mathscr{L}$ is defined as

$$\mathscr{L}\{\mathbf{J}\}(\mathbf{r}) = +\frac{\zeta_0}{i\xi}\nabla_{\mathbf{r}}\oint_{\partial V}\frac{e^{-i\xi|\mathbf{r}-\mathbf{r}'|/\ell_c}}{4\pi\,|\mathbf{r}-\mathbf{r}'|}\mathbf{J}(\mathbf{r}')\cdot\hat{\mathbf{n}}(\mathbf{r}')\,d^2\mathbf{r}' + \\ -\frac{\zeta_0}{i}\frac{\xi}{\ell_c^2}\int_V\frac{e^{-i\xi|\mathbf{r}-\mathbf{r}'|/\ell_c}}{4\pi\,|\mathbf{r}-\mathbf{r}'|}\mathbf{J}(\mathbf{r}')\,d^3\mathbf{r}'. \tag{5}$$

We can now introduce the auxiliary eigenvalue problem

$$\mathscr{L}\{\mathbf{j}_h\} = \mathcal{Z}_h\,\mathbf{j}_h, \tag{6}$$

where the eigenvalue $\mathcal{Z}_h$ represents the "radiation impedance" of the current eigenmode $\mathbf{j}_h$. The operator $\mathscr{L}$ is complex symmetric but not self-adjoint, and its spectrum has interesting features [16,17]. For any value of the size parameter ξ, its eigenvalues $\{\mathcal{Z}_h\}$ and the corresponding current eigenmodes $\{\mathbf{j}_h\}$ form infinite countable sets. Additionally, the radiation impedances are complex with positive real parts. We denote the real part of $\mathcal{Z}_h$ as "radiation resistance" $\mathcal{R}_h$, and its imaginary part as "radiation reactance" $\mathcal{X}_h$. Two modes corresponding to different eigenvalues are not orthogonal with respect to the standard scalar product, defined as follows:

$$\langle \mathbf{f},\mathbf{g}\rangle_V = \int_V \mathbf{f}^*(\mathbf{r})\cdot\mathbf{g}(\mathbf{r})\,d^3\mathbf{r}, \tag{7}$$

but they are biorthogonal, namely $\langle \mathbf{j}_h^*, \mathbf{j}_k\rangle_V = 0$, $\forall h,k\in\mathbb{N}$ with $h\neq k$ [16,17]. It is worthwhile to note that the radiation impedances and the corresponding modes depend only on the shape of the object and the size parameter ξ, not on the material properties. The eigenvalue problem (6) can be numerically solved for arbitrarily shaped objects using standard computational electromagnetic techniques, as detailed in Appendix B.

By applying Poynting's theorem in the frequency domain to the hth current mode $\mathbf{j}_h$ in free space, we can relate the radiation resistance $\mathcal{R}_h$ to the mean electromagnetic power radiated to infinity by $\mathbf{j}_h$, and the radiation reactance $\mathcal{X}_h$ to the difference between the mean magnetic and electric energies stored in the whole space. We then find [17]

$$\mathcal{R}_h = \frac{2}{\ell_c\,\|\mathbf{j}_h\|^2}\oint_{S_\infty}\mathbf{S}_h\cdot\hat{\mathbf{i}}_n = \frac{1}{\zeta_0\ell_c\,\|\mathbf{j}_h\|^2}\oint_{S_\infty}|\mathbf{E}_h|^2 dS, \tag{8a}$$

$$\mathcal{X}_h = \frac{4\omega}{\ell_c\,\|\mathbf{j}_h\|^2}W_{\rm diff}, \tag{8b}$$

where S_∞ is a spherical surface located at infinity, $\|\mathbf{j}_h\|^2 = \langle \mathbf{j}_h,\mathbf{j}_h\rangle$, $\mathbf{S}_h$ is the complex Poynting vector

$$\mathbf{S}_h = \frac{1}{2}\mathbf{E}_h\times\mathbf{H}_h^*, \tag{9}$$

$$W_{\rm diff} = \int_{\mathbb{R}^3}\left(\frac{1}{4}\mu_0\,|\mathbf{H}_h|^2 - \frac{1}{4}\varepsilon_0\,|\mathbf{E}_h|^2\right)d^3\mathbf{r}, \tag{10}$$

$\mathbf{E}_h$ and $\mathbf{H}_h$ are the electric and magnetic fields radiated by the density current mode $\mathbf{j}_h$ in free space.

We can use the current modes $\{\mathbf{j}_h\}$ to expand the solution of the nonhomogeneous scattering problem (3):

$$\mathbf{J}(\mathbf{r}) = \sum_h I_h(\omega)\,\frac{\mathbf{j}_h(\omega,\mathbf{r})}{\sqrt{\ell_c\,\langle \mathbf{j}_h^*,\mathbf{j}_h\rangle}}, \tag{11}$$

where I_h, which has the dimension of an electric current, is given by

$$I_h(\omega) = \frac{\mathcal{E}_h(\omega)}{Z_m(\omega)+\mathcal{Z}_h(\omega)}, \tag{12}$$

and $\mathcal{E}_h$, which has the dimension of a voltage, is given by

$$\mathcal{E}_h(\omega) = \frac{\langle \mathbf{j}_h^*, \mathbf{E}_{\rm inc}\rangle}{\sqrt{\ell_c\,\langle \mathbf{j}_h^*,\mathbf{j}_h\rangle}}. \tag{13}$$

It follows that the current intensity I_h is the solution of the equivalent circuit shown in Fig. 2. Unlike previous circuit models describing scattering problems involving nanoparticles, our model completely disentangles the dependencies on the excitation condition, the geometry, and the material of the object. This provides physical insights into the role of the different design parameters, and facilitates their optimization. The geometry is accounted for by the radiation impedance $\mathcal{Z}_h(\omega)$, which does not depend on the material of the object, but only on its shape and frequency. The material is accounted for by the material impedance Z_m. The excitation condition is accounted for by the voltage source, as an overlap integral with the eigenmode. We compare our circuit model with the one in Refs. [3–6] in Appendix C. This equivalent circuit enables the determination of the resonance frequency and the bandwidth of the modes, as we will show in the following.

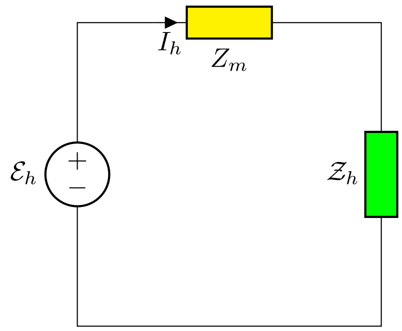

FIG. 2. Equivalent circuit modeling the response of the polarization current density mode $\mathbf{j}_h$ induced in the scatterer by the external field $\mathbf{E}_{\rm inc}$. $\mathcal{Z}_h$ is the mode's radiation impedance, Z_m is the material impedance. The voltage $\mathcal{E}_h$ of the source is given in Eq. (13). The current intensity I_h enters as an expansion coefficient in Eq. (11).

The scattering efficiency $\sigma_{\rm sca}$ [18] characterizes the power scattered by an object when illuminated by a given electromagnetic field. It is defined as the scattering cross section $C_{\rm sca}$ normalized by the geometrical cross-section G. By using expansion (11), we obtain

$$\sigma_{\rm sca}(\omega) = \frac{C_{\rm sca}}{G} = \frac{1}{G}\frac{1}{2\zeta_0\mathcal{I}_i}\oint_{S_\infty} |\mathbf{E}(\mathbf{r})|^2\, d^2\mathbf{r} \\ = \frac{1}{G}\frac{1}{2\zeta_0\mathcal{I}_i}\ell_c^2 \oint_{S_\infty} \left|\mathscr{L}\{\mathbf{J}\}\right|^2 d^2\mathbf{r}, \tag{14}$$

where $\mathcal{I}_i$ is the incident irradiance [18]. Assuming that, in the frequency interval of interest, the contribution of the hth mode to the scattering efficiency is dominant, we find

$$\sigma_{\rm sca} \approx \frac{1}{G}\frac{1}{2\zeta_0\mathcal{I}_i}\left|\frac{\mathcal{E}_h(\omega)}{Z_m(\omega)+\mathcal{Z}_h(\omega)}\right|^2 \\ \times \frac{\ell_c}{\langle \mathbf{j}_h^*, \mathbf{j}_h\rangle}\oint_{S_\infty} \left|\mathscr{L}\{\mathbf{j}_h\}\right|^2 d^2\mathbf{r}. \tag{15}$$

Since the mode $\mathbf{j}_h$ and the coupling term $\mathcal{E}_h$ vary slowly with ω, they are nonresonant terms. Therefore, the behavior of $\sigma_{\rm sca}$ near the resonance peak of the hth mode is dominated by the resonant factor $1/|Z_m(\omega)+\mathcal{Z}_h(\omega)|$. The current mode $\mathbf{j}_h$ is "tuned" to zero reactance at the resonant frequency ω_h when the imaginary part of the denominator of the resonant factor vanishes

$$X_m(\omega_h) + \mathcal{X}_h(\omega_h) = 0. \tag{16}$$

This is the resonant condition of the circuit in Fig. 2. Under this condition, the mean power scattered by the object exhibits a resonance peak near ω_h.

We emphasize that the presented circuit model, derived from the full-wave solution of Maxwell's equations, elegantly captures the resonances associated with plasmonic and dielectric nanoparticles. This model distinctly separates the contributions of excitation conditions, material dispersion, and nanoparticle geometry, offering powerful opportunities for modeling, analyzing, and optimizing their optical resonant response. In the following section, we utilize this model to examine the bandwidth of these resonances, delving into how material dispersion impacts their resonant characteristics.

III. FRACTIONAL BANDWIDTH

The resonance bandwidth is a crucial parameter for electromagnetic devices, as it characterizes their operational speed and dynamic response. In the field of radiofrequency antennas, the fractional bandwidth is a key parameter for determining the data rates that can be transmitted or received. The "fractional" bandwidth is the bandwidth of a device divided by its center frequency. It is particularly useful in telecommunications and signal processing for comparing the relative bandwidths of different signals or systems, which are directly related to the available data rates. A common definition is the 3-dB fractional bandwidth, which refers to the frequency range within which the output power is within 3 dB of its maximum value, meaning the range of frequencies over which the signal power is at least half of its peak value. Over the years its study has led to the introduction of several approximate formulas that enable its determination using experimentally accessible quantities, such as the antenna's input impedance [13,19]. These studies have also established a link between the fractional bandwidth and the quality factor of an antenna resonance, defined in terms of "observable" or "internal" stored energies [13,19–22]. Such a connection—if applicable—is particularly useful, since lower bounds to the quality factor of radiators have been developed over many years [23–34]. These explorations become particularly helpful in nanophotonics given the recent interest in ultrafast modulation of nanophotonic structures within the context of Floquet physics [35,36] and space-time metamaterials [37–39].

Referring to Fig. 3, we consider an antenna with input impedance $Z(\omega) = R(\omega) + iX(\omega)$, and a series impedance $Z_s(\omega) = R_s(\omega) + iX_s(\omega)$. The 3-dB fractional bandwidth of such an antenna, tuned at the resonance frequency ω_0, where $X_s(\omega_0) + X(\omega_0) = 0$, can be approximated using the formula derived by Yaghjian and Best [13]

$$\mathrm{FBW}_{\rm antenna} = \frac{2}{\omega_0}\frac{R_s(\omega_0)+R(\omega_0)}{\left|Z_s'(\omega_0)+Z'(\omega_0)\right|}, \tag{17}$$

where the prime indicates the derivative with respect to frequency. The derivative of the input reactance X is related to the electric and magnetic "internal" energies [13], enabling a connection to the quality factor.

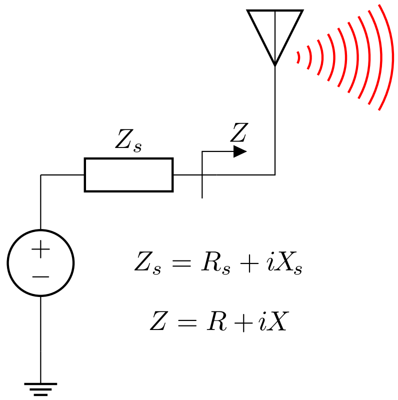

FIG. 3. Schematic representation of a transmitting antenna, featuring a feed line, input impedance $Z = R + iX$, and series impedance $Z_s = R_s + iX_s$. The antenna's fractional bandwidth can be calculated using the Yaghjian-Best formula [13].

Determining the resonance bandwidth of "nanoantennas" in the scenarios depicted in Figs. 1(a) and 1(b) follows a conceptually analogous approach to the one of classical antennas, and Eq. (17) can still be employed. However, the determination of the bandwidth of a scatterer [scenario shown in Fig. 1(c)] cannot rely on the present form of Eq. (17), because the input impedance cannot be defined without a localized feeding point. In the following, we demonstrate how the fractional bandwidth of the scattering resonances can still be evaluated by employing the circuit formulation developed in the previous section.

In order to determine the fractional bandwidth FBW_h of the scattered power spectrum σ_{sca} around the resonance frequency ω_h of the mode $\mathbf{j}_h$, following Ref. [13], we first find the two frequencies $\omega_h^{\pm} = \omega_h + \Delta\omega_h^{\pm}$ at which the scattering efficiency is $(1-\alpha)$ times its value at the resonance ω_h, where α is a parameter ranging in the interval $(0, 1)$. By assuming that, in the frequency interval of interest, the contribution of the hth mode $\mathbf{j}_h$ is dominant, we can apply Eq. (15). Since the coupling coefficient $\mathcal{E}_h$ and the mode $\mathbf{j}_h$ are weakly dependent on the frequency, we find $\omega_h^{\pm}$ by enforcing the condition

$$\frac{1}{\left|Z_m\left(\omega_h^{\pm}\right) + \mathcal{Z}_h\left(\omega_h^{\pm}\right)\right|^2} = (1-\alpha)\,\frac{1}{\left|Z_m\left(\omega_h\right) + \mathcal{Z}_h\left(\omega_h\right)\right|^2}. \tag{18}$$

Following Ref. [13], in the neighborhood of the resonance frequency it is also reasonable to assume that $\left|Z_m' + Z_m\right|^2 \gg \left(R_m'' + \mathcal{R}_h''\right)\left(R_m + \mathcal{R}_h\right)$, thus we obtain

$$\Delta\omega_h^{\pm} \approx \pm\sqrt{\beta}\,\frac{R_m\left(\omega_h\right) + \mathcal{R}_h\left(\omega_h\right)}{\left|Z_m'\left(\omega_h\right) + \mathcal{Z}_h'\left(\omega_h\right)\right|}, \tag{19}$$

where $\beta = \alpha/(1-\alpha)$. Finally, we can obtain the fractional bandwidth

$$\mathrm{FBW}_h = \frac{\Delta\omega_h^{+} - \Delta\omega_h^{-}}{\omega_h} \approx \frac{2\sqrt{\beta}}{\omega_h}\,\frac{R_m\left(\omega_h\right) + \mathcal{R}_h\left(\omega_h\right)}{\left|Z_m'\left(\omega_h\right) + \mathcal{Z}_h'\left(\omega_h\right)\right|}. \tag{20}$$

If $\alpha = 1/2$ $(\beta = 1)$ we obtain the 3-dB fractional bandwidth

$$\mathrm{FBW}_h \approx \frac{2}{\omega_h}\,\frac{R_m\left(\omega_h\right) + \mathcal{R}_h\left(\omega_h\right)}{\left|Z_m'\left(\omega_h\right) + \mathcal{Z}_h'\left(\omega_h\right)\right|}. \tag{21}$$

This is the fractional bandwidth of the circuit in Fig. 2 at the resonance frequency ω_h. We note that this formula is analogous to the Yaghjian-Best formula for the fractional bandwidth of a classical antenna [13], Eq. (17). Remarkably, our formalism allows us to derive a closed-form expression for a problem that does not involve a feeding point but instead involves excitation and observation in far field, as is common in scattering and nanophotonic problems. Here, the radiation impedance $\mathcal{Z}_h$ plays the role of the input impedance Z, while the material impedance Z_m plays the role of the series impedance Z_s. The fractional bandwidth does not depend on the excitation conditions, given that we assumed an isolated and well-defined resonant mode. Again, the contribution to the FBW_h from the geometry and from the material composition are neatly disentangled in this formulation: the geometry is accounted for by $\mathcal{Z}_h$, which does not depend on the material of the object, but only on the scatterer shape, size, and operating frequency. The material and its dispersion are accounted for by the material impedance $Z_m(\omega)$. This feature allows for the design and optimization of shape and material dispersion of plasmonic and dielectric scatterers for the desired resonant response.

IV. CIRCUIT MODEL OF PLASMONIC AND DIELECTRIC MODES

In this section, we first classify the modes of a resonator based on their behavior in the low-frequency limit. Next, we derive the asymptotic expression of the radiation impedances in both the low-frequency and high-frequency limits. Finally, we establish the Kramers-Kronig relations for radiation impedances.

Following Refs. [40], in the low-frequency limit $\xi \downarrow 0$ the eigenvalue problem (6) disentangles into two different eigenvalue problems: an *electroquasistatic* eigenvalue problem and a *magnetoquasistatic* eigenvalue problem.

The electroquasistatic current modes $\{\mathbf{j}_h^{\parallel}\}$ are the eigenmodes of the electrostatic integral operator $\mathscr{L}_e$, which gives the electrostatic field as a function of the surface charge density [41,42]:

$$\mathscr{L}_e\{\mathbf{j}_h^{\parallel}\} = \frac{1}{C_h^{\parallel}}\,\mathbf{j}_h^{\parallel}, \tag{22}$$

where

$$\mathscr{L}_e\{\mathbf{j}\} = \frac{1}{\varepsilon_0 \ell_c}\nabla_{\mathbf{r}} \oint_{\partial V} \frac{1}{4\pi\,|\mathbf{r}-\mathbf{r}'|}\mathbf{j}\left(\mathbf{r}'\right)\cdot\hat{\mathbf{n}}\left(\mathbf{r}'\right) d^2\mathbf{r}', \tag{23}$$

$C_h^{\parallel}$ is the eigenvalue, representing the “eigencapacitance” associated with the mode $\mathbf{j}_h^{\parallel}$. The eigenvalues $\{C_h^{\parallel}\}$ are discrete, real, and positive [42]. The mode $\{\mathbf{j}_h^{\parallel}\}$ and the eigenvalues $\{C_h^{\parallel}\}$ depend only on the geometry of the object. The modes $\{\mathbf{j}_h^{\parallel}\}$ are *longitudinal*: they are both irrotational and solenoidal within the object, but have non-vanishing normal components to the object surface [42]. They are also orthogonal, i.e., $\langle \mathbf{j}_h^{\parallel}, \mathbf{j}_k^{\parallel}\rangle_V = \|\mathbf{j}_h^{\parallel}\|^2\delta_{h,k}$.

Dually, the magnetoquasistatic current density modes $\{\mathbf{j}_h^{\perp}\}$ are the eigenmodes of the magnetostatic integral operator $\mathscr{L}_m$, which gives the vector potential as a function of the current density [43]:

$$\mathscr{L}_m\{\mathbf{j}_h^{\perp}\}\left(\mathbf{r}\right) = L_h^{\perp}\,\mathbf{j}_h^{\perp}\left(\mathbf{r}\right) \tag{24}$$

with

$$\mathbf{j}_h^{\perp}\left(\mathbf{r}\right)\cdot\hat{\mathbf{n}}\left(\mathbf{r}\right)\big|_{\partial V} = \mathbf{0} \quad \forall\, \mathbf{r}\in\partial V, \tag{25}$$

where

$$\mathscr{L}_m\left\{\mathbf{j}\right\}\left(\mathbf{r}\right) = \frac{\mu_0}{\ell_c}\int_V \frac{1}{4\pi\,|\mathbf{r}-\mathbf{r}'|}\mathbf{j}\left(\mathbf{r}'\right)\,d^3\mathbf{r}', \tag{26}$$

and $L_h^{\perp}$ is the eigenvalue, representing the“eigeninductance” associated to the eigenmode $\mathbf{j}_h^{\perp}$. Equation (24) holds in the weak form in the functional space of the *transverse* vector fields that are solenoidal within V and having zero normal component to ∂V, equipped with the scalar product (7). The eigenvalues are discrete, real, and positive. Furthermore, the magnetoquasistatic current modes are orthogonal $\langle \mathbf{j}_h^{\perp}|\mathbf{j}_k^{\perp}\rangle = \|\mathbf{j}_h^{\perp}\|^2\delta_{h,k}$.

A. Plasmonic modes

The “plasmonic” modes correspond to the current density modes of the full-wave operator $\mathscr{L}$, defined by Eq. (5), that tend to the electroquasistatic current modes $\mathbf{j}_h^{\parallel}$ defined by Eq. (22), in the low-frequency limit, i.e., $\xi \downarrow 0$. In this limit, their radiation impedance $\mathcal{Z}_h^{\parallel}$ tends to $(i\omega C_h^{\parallel})^{-1}$, making them “capacitive.”

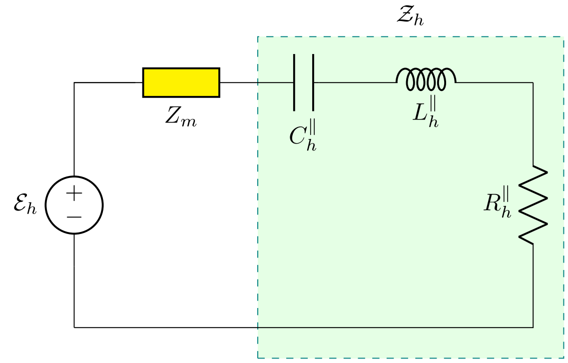

FIG. 4. Equivalent circuit for the *plasmonic* mode $\mathbf{j}_h$ in the low-frequency regime. The eigencapacitance $C_h^{\parallel}$ is defined by the eigenvalue problem (22), the resistance $R_h^{\parallel}$ and the inductance $L_h^{\parallel}$ are given by Eq. (D1).

In particular, for $\xi \ll 1$ the radiation resistance and radiation reactance are given by

$$\mathcal{R}_h = R_h^{\parallel} + \mathcal{O}\left(\frac{\omega}{c_0}\ell_c\right)^3, \tag{27a}$$

$$\mathcal{X}_h = -\frac{1}{\omega C_h^{\parallel}} + \omega L_h^{\parallel} + \mathcal{O}\left(\frac{\omega}{c_0}\ell_c\right)^2, \tag{27b}$$

where $\mathcal{O}$ is the Bachmann-Landau notation indicating the order of approximation. Interestingly, $R_h^{\parallel}$ and $L_h^{\parallel}$ can be written in closed form for arbitrarily shaped resonators in terms of the quasistatic modes, as shown in Appendix D. Equation (27b) shows that the radiation reactance can be approximated as a series connection of the capacitor $C_h^{\parallel}$ and the inductor $L_h^{\parallel}$. Thus, in the low-frequency regime, the circuit of a plasmonic mode is the one shown in Fig. 4.

In the high-frequency limit, $\xi \uparrow \infty$, it can be shown that

$$\mathcal{Z}_h \to \frac{1}{i\omega C_\infty}, \tag{28}$$

where $C_\infty = \varepsilon_0 \ell_c$.

In the Laplace domain, the radiation impedance associated with a plasmonic mode exhibits a pole at the origin of the complex plane, whereas, due to causality, no poles are present in the right semispace of the complex plane. Thus, it satisfies the Kramers-Kronig relation

$$\mathcal{X}_h\left(\omega\right) = \frac{2\omega}{\pi}\int_0^{\infty}\frac{\mathcal{R}_h\left(\Omega\right)-\mathcal{R}_h\left(\omega\right)}{\omega^2-\Omega^2}d\Omega - \frac{1}{\omega C_h^{\parallel}}. \tag{29}$$

B. Dielectric modes

Dually, “dielectric” modes are current-density modes of the full-wave operator $\mathscr{L}$ that tend to magnetoquasistatic current modes, defined by Eq. (24), in the low-frequency limit, i.e., $\xi \downarrow 0$. In this limit, their radiation admittance,

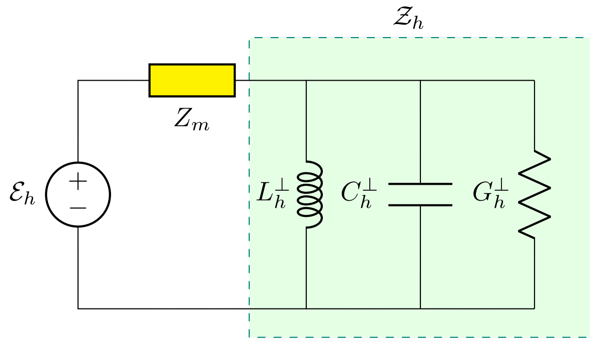

FIG. 5. Equivalent circuit for the *dielectric* mode $\mathbf{j}_h$ in the low-frequency regime. The eigeninductance $L_h^\perp$ is defined by the eigenvalue problem (24), the conductance $G_h^\perp$ and the capacitance $C_h^\perp$ are given by Eq. (D2).

i.e., the inverse of the radiation impedance $\mathcal{Y}_h = 1/\mathcal{Z}_h$, tends to $\left(i\omega L_h^\perp\right)^{-1}$, making them "inductive." In particular, for $\xi \ll 1$ the radiation conductance $\mathcal{G}_h$ and radiation susceptance $\mathcal{B}_h$ are

$$\mathcal{G}_h = G_h^\perp + \mathcal{O}\left(\frac{\omega}{c_0}\ell_c\right)^3, \tag{30a}$$

$$\mathcal{B}_h = -\frac{1}{\omega L_h^\perp} + \omega C_h^\perp + \mathcal{O}\left(\frac{\omega}{c_0}\ell_c\right)^2, \tag{30b}$$

where $G_h^\perp$ and $L_h^\perp$ have a closed form expression, provided in Appendix D. Equation (30b) shows that the radiation reactance of the hth mode results from the parallel of the capacitor $C_h^\perp$ and the inductor $L_h^\perp$. Thus, in this limit, the circuit model of a dielectric mode becomes the one shown in Fig. 5.

In the high-frequency limit, it can be shown that

$$\mathcal{Y}_h \to i\omega C_\infty, \tag{31}$$

where $C_\infty = \varepsilon_0 \ell_c$.

In the Laplace domain, the radiation admittance associated with a dielectric mode exhibits a pole at the origin of the complex plane, but no poles in the right semispace of the complex plane. Thus it satisfies the Kramer-Kronig relation

$$\mathcal{B}_h(\omega) = \frac{2\omega}{\pi}\int_0^\infty \frac{\mathcal{G}_h(\Omega) - \mathcal{G}_h(\omega)}{\omega^2 - \Omega^2} d\Omega - \frac{1}{\omega L_h^\perp}. \tag{32}$$

V. RESULTS

In order to validate the zero-reactance condition (16) and the fractional bandwidth expression (21) and demonstrate the applicability of our equivalent circuit model in fully capturing the dynamics of open resonant systems, we consider spherical objects of radius a. We begin by analyzing a metallic sphere followed by a dielectric sphere.

A. Metallic sphere

The metal response is described through a Drude susceptibility [44]

$$\chi(\omega) = -\frac{\omega_p^2}{\omega(\omega - i\nu)}, \tag{33}$$

where ω_p is the plasma frequency, and ν is the damping rate of the free electrons of the metal. We obtain the material impedance by substituting expression (33) in the definition (1),

$$Z_m(\omega) = i\omega L_m + R_m \tag{34}$$

where

$$L_m = \frac{1}{a\varepsilon_0\omega_p^2}, \quad R_m = \frac{\nu}{a\varepsilon_0\omega_p^2} = \zeta_0\frac{\nu}{\omega_p}\frac{1}{\xi_p}, \tag{35}$$

where $\xi_p = \omega_p a/c_0$ is the normalized plasma frequency. This impedance is inductive, as expected. In the following, we neglect the material losses, assuming $R_m \approx 0$. This assumption is well founded provided that the radiation losses dominate over material absorption. One of the powerful aspects of the circuit model introduced in Fig. 2 is its modularity: a change in the material of the object affects only the material impedance, without altering the radiation impedance, and, conversely, a change in geometrical shape affects only the radiation impedance. In Appendix E, we derive the material impedance for a medium described by a general Drude-Lorentz model.

For a metallic sphere, characterized by an inductive material impedance, our focus is on plasmonic modes that exhibit a capacitive radiation impedance, as we will see

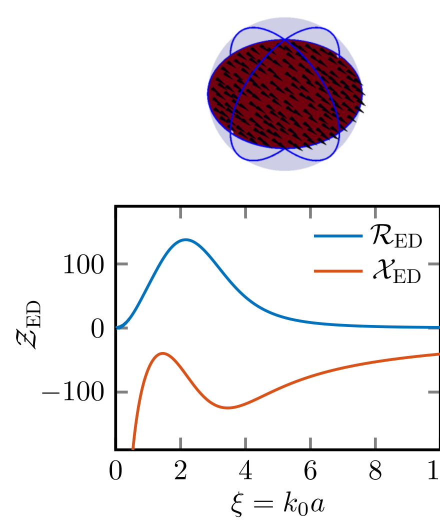

FIG. 6. Radiation resistance $\mathcal{R}_{\rm ED}$ (blue curve) and radiation reactance $\mathcal{X}_{\rm ED}$ (red curve) of the electric dipole mode $\mathbf{j}_{\rm ED}$ of a sphere of radius a as a function of the size parameter $\xi = k_0 a$.

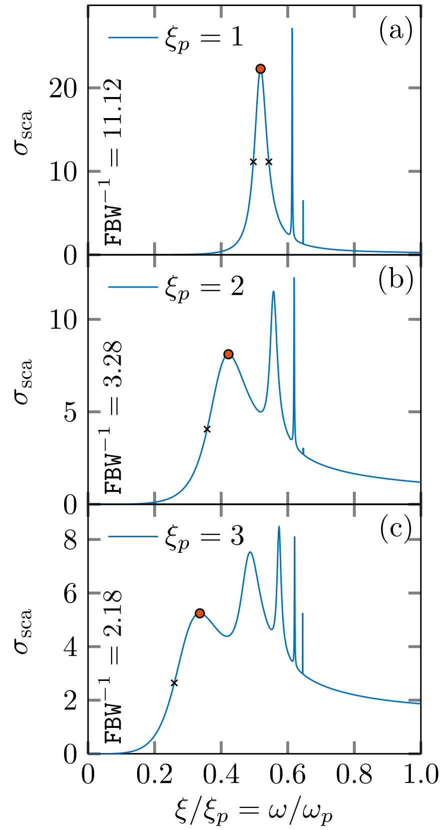

FIG. 7. Scattering efficiency σ_{sca} versus the normalized frequency ω/ω_p of a Drude metal sphere with plasma frequency ω_p, negligible material losses $\nu \approx 0$, and radius a, excited by a linearly polarized plane wave. This analysis considers three distinct values of the normalized plasma frequency $\xi_p = \omega_p a/c_0$, specifically 1 (a), 2 (b), and 3 (c). The peak corresponding to the electric dipole mode is marked with a red circle. Where applicable, 3-dB frequencies $\omega_h^{\pm}$, are shown with the symbol $\times$.

later. They include the electric dipole mode, quadrupole mode, octupole mode, etc. We begin our examination with the electric dipole mode, followed by an exploration of higher-order modes later in this section.

The dominant resonance of a metallic nanoparticle originates from the electric dipole mode $\mathbf{j}_{\text{ED}}$ [1]. The polarization current-density field of this mode is shown, in the limit $\xi \downarrow 0$, in the top portion of Fig. 6. We compute its radiation impedance $\mathcal{Z}_{\text{ED}} = \mathcal{R}_{\text{ED}} + i\mathcal{X}_{\text{ED}}$ as a function of $\xi = k_0 a$ by solving the eigenvalue problem (6). Due to the spherical symmetry, this task can be accomplished by finding the zeros of a nonlinear characteristic equation [17]. In Fig. 6, we show with a blue curve the radiation resistance $\mathcal{R}_{\text{ED}}$ versus the size parameter ξ of the particle. For $\xi \downarrow 0$, the radiation resistance $\mathcal{R}_{\text{ED}}$ vanishes. Then, as the size of the particle increases, the radiation resistance quadratically increases as $\mathcal{R}_{\text{ED}} \propto \frac{2}{9}\zeta_0\xi^2$ (see the asymptotic analysis carried out in Ref. [40]), until it reaches a maximum for $\xi = 2.15$, and eventually it goes to zero for $\xi \to \infty$. In Fig. 6, we also show with a red curve the radiation reactance $\mathcal{X}_{\text{ED}}$. For $\xi \downarrow 0$ it diverges as $-(\zeta_0/3)(1/\xi)$. As ξ increases, $\mathcal{X}_{\text{ED}}$ reaches a maximum for $\xi = 1.45$, then $\mathcal{X}_{\text{ED}}$ decreases to a minimum at $\xi = 3.44$. Eventually, it increases again, approaching asymptotically zero for $\xi \to \infty$ as $-1/(\omega C_\infty) = -\zeta_0/\xi$. The radiation reactance is always negative, so the radiation impedance of the electric dipole mode is always capacitive, regardless of the operating frequency.

The resonance frequency ω_{ED} can be derived through our circuit model, corresponding to the frequency for which the tuning condition (16) is met, corresponding to the size parameter $\xi_{\text{ED}} = \omega_{\text{ED}}\, a/c_0$. Analogously, the fractional bandwidth can be derived from Eq. (21). To validate these expressions we analyze the scattering efficiency spectrum.

In Fig. 7, we show the spectrum of the scattering efficiency σ_{sca} for several values of the normalized plasma frequency $\xi_p = \omega_p a/c_0$. The low-frequency peak, labeled with a red dot, corresponds to the electric dipole resonance. It is followed, at higher frequencies, by the resonance peaks of the electric quadrupole, octupole, and higher-order resonances. For $\xi_p \downarrow 0$, the resonance of the electric dipole mode occurs at $\xi_{\text{ED}}/\xi_p \approx 1/\sqrt{3} \approx 0.57$. An increase of ξ_p causes a redshift of the resonance position and a broadening of the peak, thus an increase in bandwidth. At $\xi_p = 2$ and $\xi_p = 3$, as illustrated in Figs. 7(b) and 7(c), respectively, the electric dipole and quadrupole partially overlap. For this reason, we compute the "exact" fractional bandwidth by finding the peak frequency ω_{peak} on the σ_{sca} curve, and the frequency ω_- at which the scattered power is one half its (first) peak value, and $\text{FBW}_h(\text{exact}) = 2(\omega_{\text{peak}} - \omega_-)/\omega_{\text{peak}}$.

In Fig. 8, the position of the first peak of σ_{sca} is compared against the resonance position obtained by enforcing the zero-reactance condition [Eq. (16)] as a

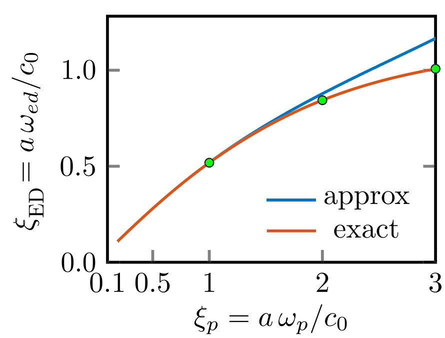

FIG. 8. Normalized frequency position of the lowest frequency peak (labeled as "exact") of the scattering efficiency spectrum of a sphere (see Fig. 7) versus the normalized plasma frequency ξ_p. This position is compared with the normalized resonance frequency (labeled as "approximate") of the electric dipole mode, determined by applying the zero-reactance condition. The green dots highlight the scenarios for $\xi_p = 1, 2, 3$ corresponding to panels (a)–(c) of Fig. 7.

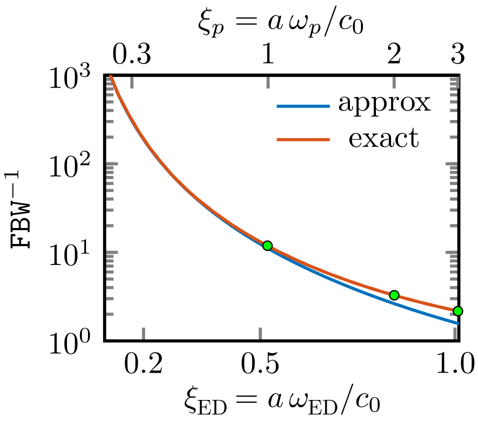

FIG. 9. Inverse value of the "exact" fractional bandwidth evaluated from the scattering efficiency spectrum of a metallic sphere (see Fig. 7), as explained in the text, versus the size parameter at the resonance $a\omega_{\mathrm{ED}}/c_0$ (bottom axis) and normalized plasma frequency $a\omega_p/c_0$ (top axis). The inverse of the exact fractional bandwidth is compared against the inverse of the "approximate" fractional bandwidth of the electric dipole mode given by Eq. (21). The green dots highlight the scenarios for $\xi_p = 1, 2, 3$ corresponding to panels (a)–(c) of Fig. 7.

function of the normalized plasma frequency $\xi_p = \omega_p a/c_0$. A very good agreement is generally observed, with a slight disagreement beginning to emerge when the normalized plasma frequency ξ_p exceeds 2. This is attributed to the increasing weight of the radiation resistance $\mathcal{R}_{\mathrm{ED}}$, whose contribution is neglected by the zero-reactance condition. In the low-frequency regime, $\mathcal{R}_{\mathrm{ED}}$ quadratically increases with frequency, causing a low-frequency shift in the position of the actual scattering peak relative to the prediction made under the zero-reactance condition.

The "exact" fractional bandwidth and the "approximated" fractional bandwidth, given by Eq. (21), are compared in Fig. 9 as a function of the resonance size parameter ξ_{ED} (bottom axis). Each value of ξ_{ED} is associated with a different value of normalized plasma frequency ξ_p (top axis). We observe very good agreement, with a small deviation emerging when the normalized plasma frequency ξ_p exceeds 2, attributable to the slight discrepancy in identifying the resonance frequency.

The analysis carried out so far refers to the full-wave regime. Nevertheless, the low-frequency regime, achieved when $\xi \ll 1$, is the most relevant for plasmonic resonances. In this regime, the circuit model for the electric dipole mode is shown in Fig. 10. The material impedance, enclosed in the yellow box, is given by the series of the kinetic material inductance and the material resistance, as specified by Eq. (34). The radiation impedance of the mode, enclosed in the green box, is the series of the eigencapacitance $C^{\parallel}_{\mathrm{ED}}$, eigenvalue of the problem (22), the radiation resistance $\mathcal{R}^{\parallel}_{\mathrm{ED}}$, and the inductance $L^{\parallel}_{\mathrm{ED}}$, given

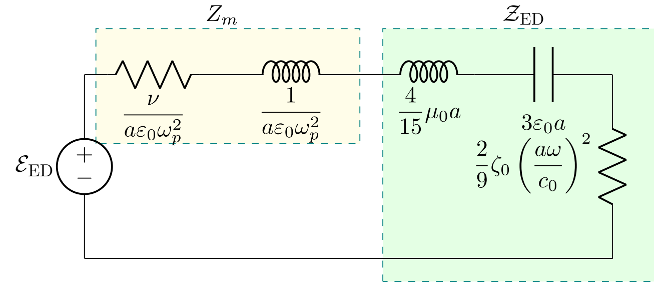

FIG. 10. Equivalent circuit describing the response of the electric dipole mode $\mathbf{j}_{\mathrm{ED}}$ in a Drude metal sphere (with plasma frequency ω_p, damping rate ν, and radius a), in the low-frequency limit. Z_m is the material impedance. $\mathcal{Z}_{\mathrm{ED}}$ is the radiation impedance of the electric dipole mode.

by Eq. (D1) in Appendix D. For a sphere, these quantities have analytical expressions

$$C^{\parallel}_{\mathrm{ED}} = 3\varepsilon_0 a, \quad \mathcal{R}^{\parallel}_{\mathrm{ED}}(\xi) = \frac{2}{9}\zeta_0\left(\frac{a\omega}{c_0}\right)^2, \quad L^{\parallel}_{\mathrm{ED}} = \frac{4}{15}\mu_0 a. \tag{36}$$

The resonance frequency of the LC circuit in Fig. 10 is given by

$$\omega_{\mathrm{ED}} = \frac{1}{\sqrt{(L_m + L^{\parallel}_{\mathrm{ED}})C^{\parallel}_{\mathrm{ED}}}}. \tag{37}$$

which in the limit $\xi_p \ll 1$ returns

$$\omega_{\mathrm{ED}} \approx \frac{\omega_p}{\sqrt{3}}\left[1 - \frac{2}{15}\left(\frac{a\omega_p}{c_0}\right)^2\right] \approx \frac{\omega_p}{\sqrt{3}}. \tag{38}$$

This is a well-known result in the field of plasmonics [1,45], and can also be obtained using the circuit model introduced by Engheta and coworkers [3]. In Appendix C, we compare both models. The approximate 3-dB fractional bandwidth is obtained from Eq. (21),

$$\mathrm{FBW}_{\mathrm{ED}} \approx \frac{2}{\omega_{\mathrm{ED}}}\frac{R_m(\omega_{\mathrm{ED}}) + \mathcal{R}_{\mathrm{ED}}(\omega_{\mathrm{ED}})}{\left|Z'_m(\omega_{\mathrm{ED}}) + \mathcal{Z}'_h(\omega_{\mathrm{ED}})\right|} = \frac{2}{3}\left(\frac{a\omega_{\mathrm{ED}}}{c_0}\right)^3, \tag{39}$$

which equates the inverse of the minimum Q factor of a small radiator of the electric-type [23,28,34,46]. This equation succinctly illustrates the well-known trade-off between bandwidth and the size of the resonator, demonstrating that a reduction in size will correspondingly decrease the resonance bandwidth. Formula (21) is also applicable in scenarios where material losses are comparable to radiation losses. In such instances, a closer examination of its numerator reveals that the total fractional bandwidth can be approximated by summing the

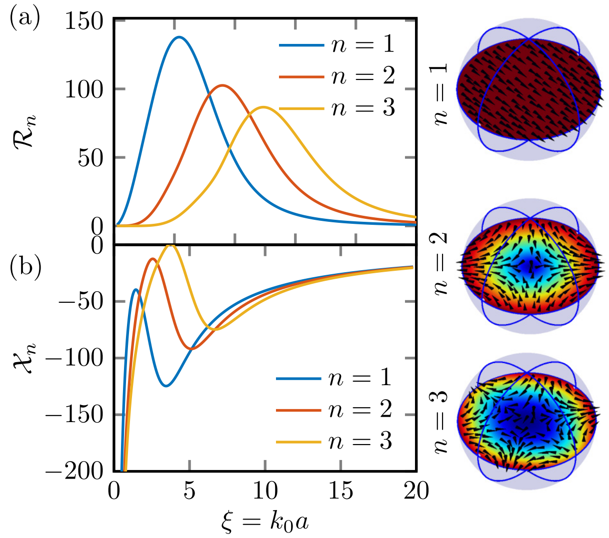

FIG. 11. (a) Radiation resistance $\mathcal{R}_n$ and (b) radiation reactance $\mathcal{X}_n$ of selected plasmonic modes of a sphere of radius a as a function of the size parameter $\xi = k_0 a$: electric dipole mode ($n = 1$), electric quadrupole mode ($n = 2$), and electric octupole mode ($n = 3$).

fractional bandwidths attributed to material resistance and radiation resistance, respectively. In Appendix E, the analogous circuit for a Drude-Lorentz sphere is shown and investigated.

The circuit model of Fig. 2 also applies to higher-order plasmonic resonances. In Figs. 11(a) and 11(b), we show, as a function of the size parameter $\xi = k_0 a$, the radiation resistance $\mathcal{R}_n$ and the radiation reactance $\mathcal{X}_n$ of plasmonic modes of different multipolar order n, namely the electric dipole mode ($n = 1$), the electric quadrupole mode ($n = 2$), and the electric octupole mode ($n = 3$). The polarization current-density field of these modes is shown on the right side of Fig. 11. The eigenspace corresponding to the eigenvalue $\mathcal{Z}_n$ of the problem (6) is spanned by the polarization current-density modes

$$\mathbf{j}_{\substack{e\\o}nm} = \mathbf{N}^{(1)}_{\substack{e\\o}mn}\left(\xi \frac{\mathbf{r}}{a}\sqrt{1 + i\frac{\zeta_0}{\mathcal{Z}_n \xi}}\right), \tag{40}$$

where the functions $\mathbf{N}^{(1)}_{\substack{e\\o}mn}$ are the vector spherical wave functions regular at the origin (we follow the definition of Ref. [18]), the subscripts e and o denote even and odd azimuthal dependence, and $m = 0, \cdots, n$. The functions $\mathbf{N}^{(1)}_{\substack{e\\o}mn}$ exhibit zero radial magnetic field. Overall, the behavior of the radiation resistance and reactance of the electric quadrupole and the octupole looks similar to the ones of the electric dipole mode, investigated in the previous section. Nevertheless, the maxima and minima of the curves shift at higher values of the size parameter as the multipolar order n of the mode increases.

In the low-frequency regime, the radiation resistance and reactance of plasmonic modes can be written accordingly to Eq. (27), where

$$R_n^{\|} = \zeta_0 \frac{(n+1)}{[(2n+1)!!]^2}\left(\frac{a\omega}{c_0}\right)^{2n}, \tag{41a}$$

$$C_n^{\|} = \frac{2n+1}{n}\varepsilon_0 a, \tag{41b}$$

$$L_n^{\|} = \frac{2(n+1)}{(3+2n)(4n^2-1)}\mu_0 a. \tag{41c}$$

The above parameters specify the circuit model of plasmon modes in the low-frequency regime, shown in Fig. 4. The approximate 3-dB fractional bandwidth, in the low-frequency regime, is obtained by substituting the expressions (41) and (35) into Eq. (21):

$$\mathrm{FWB}_n = \frac{(n+1)(2n+1)}{n[(2n+1)!!]^2}\left(\frac{a\omega_n}{c_0}\right)^{2n+1}. \tag{42}$$

For instance, for electric quadrupole and octupole modes, we have, respectively,

$$\mathrm{FWB}_2 = \frac{1}{30}\left(\frac{a\omega_2}{c_0}\right)^5; \quad \mathrm{FWB}_3 = \frac{4}{4725}\left(\frac{a\omega_3}{c_0}\right)^7. \tag{43}$$

These results align with those found in previous works [47–49]. Our circuit model offers a robust framework for separately analyzing the influence of radiation and material losses on the characteristics of plasmonic resonances. Specifically, we can examine the ratio of radiation to material resistance, expressed as

$$\frac{R_n^{\|}}{R_m} = \frac{(n+1)}{[(2n+1)!!]^2}\frac{\xi_p}{(\nu/\omega_p)}\xi^{2n}, \tag{44}$$

where we employ Eqs. (35) and (41a). The above formula highlights that, in the low-frequency regime, as the multipolar order, n, of the plasmonic mode increases, the radiation resistance diminishes relative to the material resistance, given specific values of ξ, ξ_p, and ν/ω_p.

B. Dielectric sphere

A second significant scenario for nanophotonics is the case of all-dielectric scatterers [50–52], which exhibit even richer behavior due to the ease of exciting multipolar resonances and engineering interference effects. Specifically, we apply our formulation and circuit model to a dielectric sphere described by the Debye susceptibility [53,54]:

$$\chi(\omega) = \frac{\chi_0}{1 + i\omega/\gamma}, \tag{45}$$

where χ_0 is the zero-frequency susceptibility and γ is the relaxation frequency. By the definition (1), the material impedance is

$$Z_m = \frac{1}{i\omega C_m} + R_m, \tag{46}$$

where C_m is the material capacity

$$C_m = \varepsilon_0 \chi_0 a, \tag{47}$$

and

$$R_m = \zeta_0 \frac{1}{\chi_0}\left(\frac{c_0}{a\gamma}\right) = \frac{1}{C_m\,\gamma}, \tag{48}$$

In the low-dissipation limit, $\omega \ll \gamma$, the material admittance, Y_m, reciprocal of material impedance Z_m, can be approximated as

$$Y_m(\omega) \approx G_m + i\omega C_m, \tag{49}$$

where G_m is the material conductance

$$G_m = \left(\frac{\omega}{\gamma}\right)^2 \frac{1}{R_m} = \frac{1}{\zeta_0}\chi_0\left(\frac{c_0}{\gamma a}\right)\xi^2. \tag{50}$$

In the following, we neglect material losses, assuming $R_m \approx 0$. Since the material impedance is capacitive, a dielectric sphere cannot support the resonance of plasmonic modes, whose radiation reactance, as shown in Figs. 6 and 11, is always capacitive, and therefore, the zero-reactance condition would never be satisfied.

For a dielectric sphere, characterized by a capacitive material impedance, our focus is on dielectric modes that exhibit an inductive radiation impedance at low frequencies. We begin our examination with the magnetic dipole mode, while higher-order modes will be explored later in this section.

The polarization current-density field of the magnetic dipole mode $\mathbf{j}_{\mathrm{MD}}$ is shown in the top portion of Fig. 12 for $\xi \downarrow 0$. The radiation impedance $\mathcal{Z}_{\mathrm{MD}} = \mathcal{R}_{\mathrm{MD}} + i\mathcal{X}_{\mathrm{MD}}$ of the magnetic dipole mode is computed as a function of the size parameter $\xi = k_0 a$ by solving the eigenvalue problem (6). Figure 12 shows the radiation resistance $\mathcal{R}_{\mathrm{MD}}$ and the radiation reactance $\mathcal{X}_{\mathrm{MD}}$ as a function of the size parameter. For $\xi \downarrow 0$, $\mathcal{R}_{\mathrm{MD}}$ vanishes, then it grows as $(2\zeta_0/\pi^4)\xi^4$ reaching a maximum for $\xi = 3.5$; eventually it decreases and goes to zero as $\xi \to \infty$. For $\xi \downarrow 0$, $\mathcal{X}_{\mathrm{MD}}$ vanishes, then it linearly grows as $(\zeta_0/\pi^2)\xi$. The radiation reactance is inductive for $\xi < 3.4$, while for larger size parameters it becomes capacitive. This implies that the magnetic dipole mode can be tuned to resonance in dielectric particles for values of a, which are not too large compared to the wavelength.

We validate our circuit model by predicting the resonance position of the magnetic dipole mode, its dispersion,

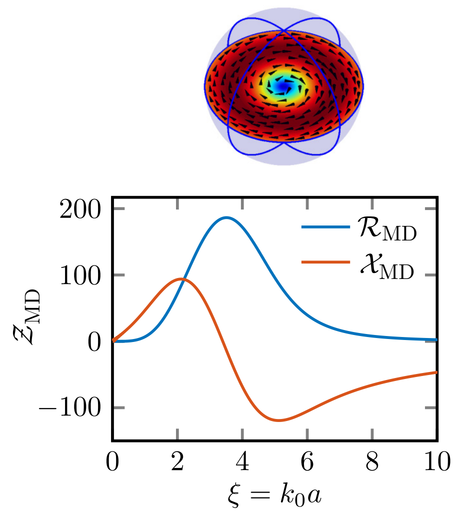

FIG. 12. Radiation resistance $\mathcal{R}_{\mathrm{MD}}$ (blue curve) and reactance $\mathcal{X}_{\mathrm{MD}}$ (red curve) of the magnetic dipole mode $\mathbf{j}_{\mathrm{MD}}$ of a sphere of radius a as a function of the size parameter $\xi = k_0 a$.

and its bandwidth. We indicate with ω_{MD} the value of the frequency for which the tuning condition (16) is verified and with $\xi_{\mathrm{MD}} = \omega_{\mathrm{MD}}\, a/c_0$ the corresponding size parameter. In Fig. 13, we show the spectrum of the scattering efficiency σ_{sca} as a function of $\xi\sqrt{\chi_0} = k_0 a\sqrt{\chi_0}$ for several values of the susceptibility χ_0. The low-frequency peak, labeled with a red dot, corresponds to the resonance of the magnetic dipole. It is followed, at higher frequencies, by the resonance peaks of the higher-order modes. For $\chi_0 \uparrow \infty$, the resonance of the magnetic dipole mode occurs at $\xi_{\mathrm{MD}}\sqrt{\chi_0} \approx \pi$. A decrease of χ_0 causes a redshift of the resonance position and a broadening of the peak, thus an increase in the bandwidth. In Fig. 14, the peak position of σ_{sca} is compared against the resonance position obtained by enforcing the zero-reactance condition [Eq. (16)] as a function of the susceptibility of the sphere χ_0. Excellent agreement is found. The "exact" fractional bandwidth and the "approximated" fractional bandwidth, given by Eq. (21), are compared in Fig. 15 as a function of the size parameter ξ_{MD} at the magnetic dipole resonance (bottom x axis). Each value of ξ_{MD} corresponds to a different susceptibility, χ_0, of the sphere (indicated on the top axis). Remarkably, we observe very good agreement even when the particle size is comparable to the resonance wavelength of the magnetic dipole mode.

It is interesting to evaluate the expression of the resonance frequency and the fractional bandwidth of the magnetic dipole mode in the low-frequency limit. In the limit $\xi \downarrow 0$, the radiation resistance $\mathcal{R}_{\mathrm{MD}}$ and radiation reactance $\mathcal{X}_{\mathrm{MD}}$ have the asymptotic expression (30) where

$$\mathcal{G}^{\perp}_{\mathrm{MD}} = \frac{2}{\zeta_0}\xi^2, \quad L^{\perp}_{\mathrm{MD}} = \frac{1}{\pi^2}\mu_0 a, \quad C^{\perp}_{\mathrm{MD}} = 3\varepsilon_0 a. \tag{51}$$

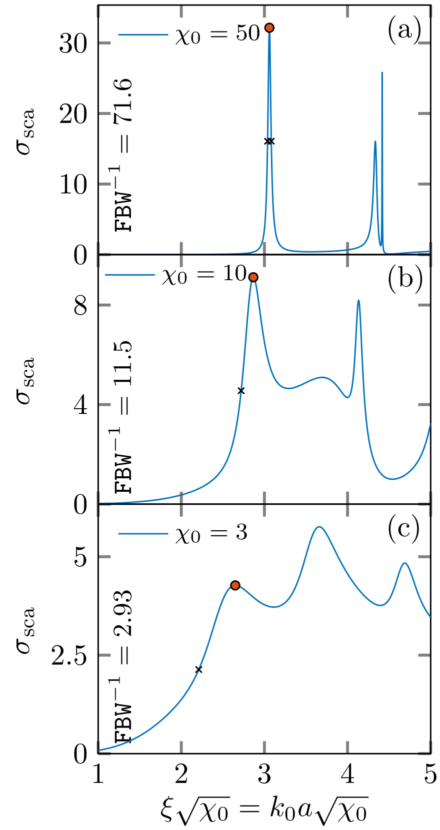

FIG. 13. Scattering efficiency σ_{sca} plotted against the normalized size parameter $\xi\sqrt{\chi_0}$ for a Debye dielectric sphere with zero-frequency susceptibility χ_0, in the low-dissipation limit, and having radius a, when excited by a linearly polarized plane wave. This analysis considers three distinct values of χ_0: 50 (a), 10 (b), and 3 (c). The peak corresponding to the magnetic dipole mode is labeled with a red circle. Where applicable, the 3-dB frequencies $\omega_{\text{MD}}^{\pm}$ are shown with the symbol $\times$.

The resonant frequency ω_{MD} can be calculated directly from the circuit model

$$\omega_{\text{MD}} = \frac{1}{\sqrt{L_{\text{MD}}^{\perp}(C_m + C_{\text{MD}}^{\perp})}} \approx \frac{c_0}{a}\frac{\pi}{\sqrt{\chi_0}}\left(1 - \frac{3}{2}\frac{1}{\chi_0}\right). \tag{52}$$

The approximate 3-dB fractional bandwidth is given by Eq. (21),

$$\text{FBW}_{\text{approx}} = \frac{2}{\omega_{\text{MD}}}\frac{R_m(\omega_{\text{MD}}) + \mathcal{R}_{\text{MD}}(\omega_{\text{MD}})}{\left|Z_m'(\omega_{\text{MD}}) + \mathcal{Z}_{\text{MD}}'(\omega_{\text{MD}})\right|} = \frac{2}{\pi^2}\left(\frac{\omega_{\text{MD}} a}{c_0}\right)^3, \tag{53}$$

which agrees with previous derivations [40]. This formula reveals a trade-off between the bandwidth and the size of the resonator, showing that a reduction in size will correspondingly decrease the resonance bandwidth. Unlike the

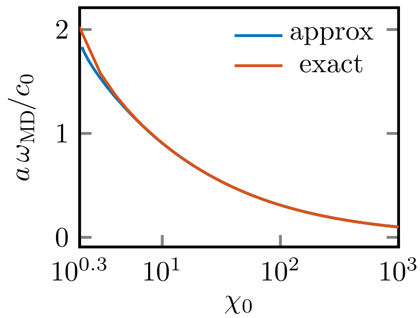

FIG. 14. Normalized frequency position of the lowest frequency peak (labeled as "exact") of the scattering efficiency spectrum of a Debye dielectric sphere with zero-frequency susceptibility χ_0, in the low-dissipation limit, and with radius a (see Fig. 13) versus χ_0. This peak position is compared with the normalized resonance frequency of the magnetic dipole mode (labeled as "approximate") obtained by enforcing the zero-reactance condition.

case of a metallic sphere, this bandwidth does not equate to the inverse of the minimum Q factor for resonators of the magnetic type [23,28,34,46]. This limit scales as $\frac{1}{3}(\omega_{\text{MD}} a/c_0)^3$ and is attained with a spherical shell inductor, as explored in the works of Thal [27] and subsequent authors [28,34,46].

Now, we consider high-order dielectric modes of the sphere. Due to symmetry, the dielectric modes of a sphere are divided into two complementary subsets: the ones of "E-type," and the ones of "H-type."

The radiation impedances $\mathcal{Z}_{n\ell}^{H\text{-type}}$ of the H-type dielectric modes of a sphere are indexed by the two

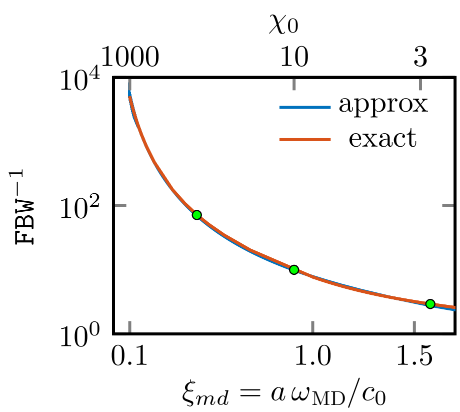

FIG. 15. Inverse value of the "exact" fractional bandwidth evaluated from the scattering efficiency spectrum of a Debye dielectric sphere (see Fig. 13), as explained in the text, versus its susceptibility χ_0 (top x axis), and of the corresponding size parameter ξ_{MD} at the resonance position of the magnetic dipole (bottom x axis). The inverse of the exact fractional bandwidth is compared against the inverse of the "approximate" fractional bandwidth of the magnetic dipole mode given by Eq. (21). The green dots highlight the scenarios for $\chi_0 = 50, 10, 3$ corresponding to panels (a)–(c) of Fig. 13.

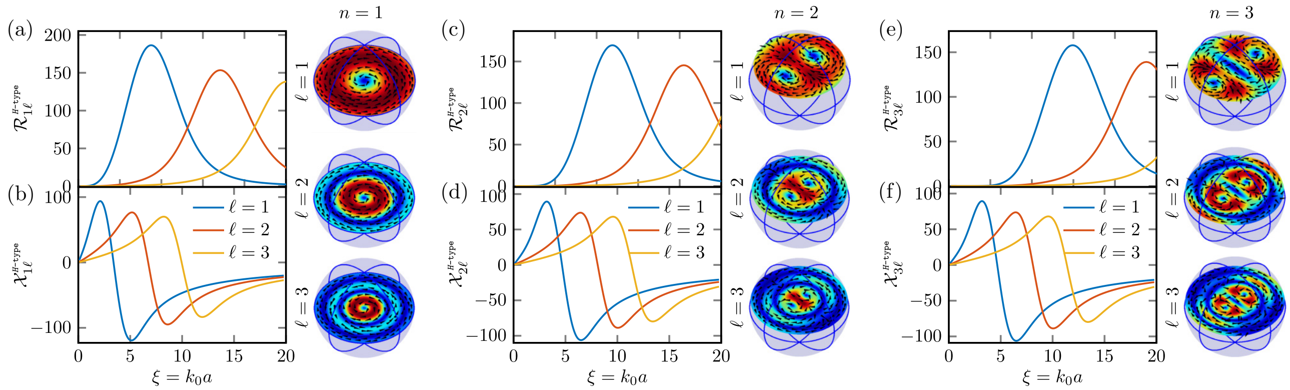

FIG. 16. Radiation resistance $\mathcal{R}_{n\ell}^{H\text{-type}}$ and reactance $\mathcal{X}_{n\ell}^{H\text{-type}}$ of the H-type dielectric modes of a sphere of radius a as a function of the size parameter $\xi = k_0 a$ for multipolar orders $n = 1$ (a)–(b), $n = 2$ (c)–(d), $n = 3$ (e)–(f), and for several values of the index ℓ.

integers $n = 1, 2, 3, \ldots$ and $\ell = 1, 2, 3, \ldots$. The eigenspace corresponding to the eigenvalue $\mathcal{Z}_{n\ell}^{H\text{-type}}$ is spanned by the current density modes:

$$\mathbf{j}_{\substack{e\\o}nm\ell}^{H\text{-type}} = \mathbf{M}_{\substack{e\\o}mn}^{(1)}\left(\xi\frac{\mathbf{r}}{a}\sqrt{1 + i\frac{\zeta_0}{\mathcal{Z}_{n\ell}^{H\text{-type}}\xi}}\right). \tag{54}$$

Each mode $\mathbf{j}_{\substack{e\\o}nm\ell}^{H\text{-type}}$ exhibits a zero radial electric field, which is why we denote them as H-type dielectric modes. These include magnetic dipole modes ($n = 1$), magnetic quadrupole modes ($n = 2$), magnetic octupole modes ($n = 3$), and so on.

The radiation impedances $\mathcal{Z}_{n\ell}^{E\text{-type}}$ of the E-type dielectric modes of a sphere can be indexed by the two integers $n = 1, 2, 3, \ldots$ and $\ell = 1, 2, 3, \ldots$. The eigenspace corresponding to the eigenvalue $\mathcal{Z}_{n\ell}^{E\text{-type}}$ is spanned by the current-density modes

$$\mathbf{j}_{\substack{e\\o}nm\ell}^{E\text{-type}} = \mathbf{N}_{\substack{e\\o}mn}^{(1)}\left(\xi\frac{\mathbf{r}}{a}\sqrt{1 + i\frac{\zeta_0}{\mathcal{Z}_{n\ell}^{E\text{-type}}\xi}}\right). \tag{55}$$

Each mode $\mathbf{j}_{\substack{e\\o}nm\ell}^{E\text{-type}}$ exhibits zero radial magnetic field, which is why we denote them as E-type dielectric modes. These include electric toroidal dipole modes ($n = 1$), electric toroidal quadrupole modes ($n = 2$), and so on.

In Eqs. (54) and (55), the functions $\mathbf{M}_{\substack{e\\o}mn}^{(1)}$ and $\mathbf{N}_{\substack{e\\o}mn}^{(1)}$ are the vector spherical wave functions regular at the origin (we follow the definition of Ref. [18]); the radial number ℓ gives the number of maxima of the magnitude of these modes along $\hat{\mathbf{r}}$ inside the sphere; the subscripts e and o denote even and odd azimuthal dependence; $n = 1, 2, 3, \ldots$ is the multipolar order of the mode; and $m = 0, \ldots, n$, which are shown on the right.

In Fig. 16, we show the radiation resistance $\mathcal{R}_{n\ell}^{H\text{-type}}$ and the radiation reactance $\mathcal{X}_{n\ell}^{H\text{-type}}$ versus the size parameter ξ for dielectric modes of the H-type with multipolar order $n = 1$ (a)–(b), $n = 2$ (c)–(d), $n = 3$ (e)–(f). The polarization current-density field of these modes is shown on the right of the corresponding panels. Overall, the behavior of $\mathcal{R}_{n\ell}^{H\text{-type}}$ and $\mathcal{X}_{n\ell}^{H\text{-type}}$ resembles that of the magnetic dipole mode, with a shift at higher frequencies as the indices n and ℓ increase. In the low-frequency limit, the radiation conductance and radiation susceptance of H-type dielectric modes can be expressed accordingly to Eq. (30), where the conductance, inductance, and capacitance are given by

$$G_{n\ell}^{H\text{-type}} = \frac{1}{\zeta_0}\frac{2}{[(2n-1)!!]^2}\left(\frac{a\omega}{c_0}\right)^{2n}, \tag{56a}$$

$$L_{n\ell}^{H\text{-type}} = \frac{1}{(z_{n-1,\ell})^2}\,\mu_0 a, \tag{56b}$$

$$C_{n\ell}^{H\text{-type}} = \frac{2n+1}{2n-1}\,\varepsilon_0 a, \tag{56c}$$

and $z_{n\ell}$ is the ℓth zero of the spherical Bessel function j_n. The parameters given by Eqs. (56) completely specify the radiation impedance enclosed in the green box of the circuit model shown in Fig. 5. The approximate 3-dB fractional bandwidth of an H-type dielectric mode resonating at the frequency $\omega_{n\ell}^{H\text{-type}}$ is obtained, in the low frequency limit, by substituting the expressions (56) and (49) in Eq. (21):

$$\mathrm{FBW}_{n\ell}^{H\text{-type}} = \frac{2}{\left[z_{n-1,\ell}\,(2n-1)!!\right]^2}\left(\frac{a\omega_{n\ell}^{H\text{-type}}}{c_0}\right)^{2n+1}. \tag{57}$$

For example, for the magnetic dipole mode ($n = 1$) with $\ell = 2$ and for the magnetic quadrupole mode ($n = 2$) with

$\ell = 1$, the calculations yield

$$\mathrm{FBW}_{1,2}^{H\text{-type}} = \frac{2}{z_{0,2}^2}\left(\frac{a\omega_{1,1}^{H\text{-type}}}{c_0}\right)^3 \approx \frac{1}{19.74}\left(\frac{a\omega_{1,1}^{H\text{-type}}}{c_0}\right)^3,$$
$$\mathrm{FBW}_{2,1}^{H\text{-type}} = \frac{2}{9z_{1,1}^2}\left(\frac{a\omega_{2,1}^{H\text{-type}}}{c_0}\right)^5 \approx \frac{1}{90.8}\left(\frac{a\omega_{2,1}^{H\text{-type}}}{c_0}\right)^5. \tag{58}$$

These fractional bandwidths exhibit the same dependence on the resonant frequency as the plasmonic electric dipole and quadrupole modes, respectively, albeit with smaller coefficients. Moreover, it is crucial to understand that the radial index ℓ does not affect the power dependence of the fractional bandwidth, which is determined solely by the multipolar order, but influences only the multiplicative prefactor.

In this dielectric scenario, our circuit model provides a robust framework for effectively comparing radiation and material losses. In the low-frequency limit, this comparison is quantified by evaluating the ratio of the radiation conductance associated with H-type dielectric modes to the conductance of the material:

$$\frac{G_{n\ell}^{H\text{-type}}}{G_m} = \frac{2}{[(2n-1)!!]^2}\left(\frac{a\gamma}{c_0}\right)\frac{1}{\chi_0}\xi^{2n-2}. \tag{59}$$

A ratio less than one indicates that radiation losses dominate, while a ratio greater than one suggests that material losses are more significant. This ratio is influenced by the $(2n-2)$th power of the size parameter, ξ, and the prefactor, which diminishes as the multipolar order n increases.

In Fig. 17, we plot the radiation resistance $\mathcal{R}_{n\ell}^{E\text{-type}}$ and the radiation reactance $\mathcal{X}_{n\ell}^{E\text{-type}}$ versus the size parameter ξ for the E-type dielectric modes with multipolar order $n = 1$ (a)–(b), $n = 2$ (c)–(d), and $n = 3$ (e)–(f). The polarization current-density field of these modes is shown on the right side of the corresponding panels. Overall, the behavior of $\mathcal{R}_{n\ell}^{E\text{-type}}$ and $\mathcal{X}_{n\ell}^{E\text{-type}}$ qualitatively resembles that of the magnetic dipole mode. However, the curves shift at higher frequencies as the indices n and ℓ increase.

In the low-frequency regime, the radiation conductance and radiation susceptance of E-type dielectric modes can be expressed accordingly to Eq. (30), where the conductance, inductance, and capacitance are given by

$$G_{n\ell}^{E\text{-type}} = \frac{1}{\zeta_0}\frac{n^2}{[(2n-1)!!]^2}\left(\frac{a\omega}{c_0}\right)^{2n+2}, \tag{60a}$$

$$L_{n\ell}^{E\text{-type}} = \frac{1}{(z_{n,\ell})^2}\mu_0 a, \tag{60b}$$

$$C_{n\ell}^{E\text{-type}} = \frac{n+2}{n}\varepsilon_0 a. \tag{60c}$$

The parameters given by Eqs. (60) completely specify the radiation impedance enclosed in the green box of the circuit model shown in Fig. 5 for any E-type dielectric mode. The 3-dB approximate fractional bandwidth of the E-type dielectric mode resonating at the frequency $\omega_{n\ell}^{E\text{-type}}$ is obtained by substituting the expressions (60) and (49) in Eq. (21):

$$\mathrm{FBW}_{n\ell}^{E\text{-type}} = \frac{2}{\left[n\, z_{n,\ell}\,(2n-1)!!\right]^2}\left(\frac{a\omega_{n\ell}^{E\text{-type}}}{c_0}\right)^{2n+3}. \tag{61}$$

For the dielectric toroidal electric dipole mode ($n = 1$) with $\ell = 1$ and for the toroidal electric quadrupole mode ($n = 2$) with $\ell = 1$, we have

$$\mathrm{FBW}_{1,1}^{E\text{-type}} = \frac{2}{z_{1,1}^2}\left(\frac{a\omega_{1,1}^{E\text{-type}}}{c_0}\right)^5 \approx \frac{1}{10.1}\left(\frac{a\omega_{1,1}^{E\text{-type}}}{c_0}\right)^5,$$
$$\mathrm{FBW}_{2,1}^{E\text{-type}} = \frac{1}{18\, z_{2,1}^2}\left(\frac{a\omega_{2,1}^{E\text{-type}}}{c_0}\right)^7 \approx \frac{1}{598}\left(\frac{a\omega_{2,1}^{E\text{-type}}}{c_0}\right)^7. \tag{62}$$

Significantly, the fractional bandwidths of the toroidal electric dipole and toroidal electric quadrupole scale with the resonant size parameter to the fifth and seventh powers, respectively. In contrast, the fractional bandwidths of plasmonic electric dipoles and quadrupoles scale to lower powers of the size parameter, specifically the third and fifth powers, respectively. The radial index ℓ does not affect the power dependence of the fractional bandwidth, which is determined solely by the multipolar order n; it influences only the multiplicative prefactor.

In this case as well, the comparison between radiation and material losses can be carried out in the low-frequency regime by examining the ratio of the radiation conductance associated with E-type dielectric modes to the conductance of the material in question. The formula for this ratio is given by

$$\frac{G_{n\ell}^{E\text{-type}}}{G_m} = \frac{n^2}{[(2n-1)!!]^2}\left(\frac{a\gamma}{c_0}\right)\frac{1}{\chi_0}\xi^{2n}. \tag{63}$$

The difference with dielectric modes of the magnetic type is that this ratio scales with an even higher power, i.e., $2n$, of the size parameter.

VI. DISCUSSION

In this work, we derived from first principles a circuit model for open electromagnetic resonators in the full-wave

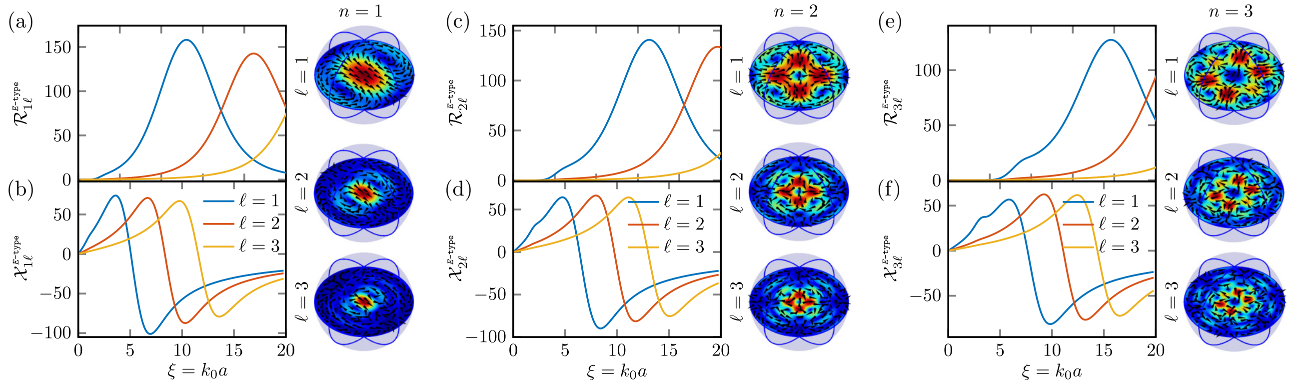

FIG. 17. Radiation resistance $\mathcal{R}_{n\ell}^{E\text{-type}}$ and reactance $\mathcal{X}_{n\ell}^{E\text{-type}}$ of the E-type dielectric modes of a sphere of radius a as a function of the size parameter $\xi = k_0 a$ for multipolar orders $n = 1$ (a)–(b), $n = 2$ (c)–(d), $n = 3$ (e)–(f) and several values of the index ℓ.

regime. This model allows us to associate an effective "material impedance" $Z_m(\omega) = R_m(\omega) + iX_m(\omega)$ with the susceptibility of the material composing the scatterer. The polarization current density $\mathbf{J}$ induced in the object by an arbitrary external field $\mathbf{E}_{\text{inc}}$ is expanded in terms of a discrete set of polarization current density modes $\{\mathbf{j}_h\}_{h\in\mathbb{N}}$ as

$$\mathbf{J}(\mathbf{r}) = \sum_h \frac{\mathcal{E}_h(\omega)}{Z_m(\omega) + \mathcal{Z}_h(\omega)} \frac{\mathbf{j}_h(\omega, \mathbf{r})}{\sqrt{\ell_c \langle \mathbf{j}_h^*, \mathbf{j}_h\rangle}},$$

where ℓ_c is a characteristic linear dimension of the object, $\mathcal{E}_h(\omega) = \langle \mathbf{j}_h^*, \mathbf{E}_{\text{inc}}\rangle / \sqrt{\ell_c \langle \mathbf{j}_h^*, \mathbf{j}_h\rangle}$ is the overlap integral between the hth mode $\mathbf{j}_h$ and the incident electric field $\mathbf{E}_{\text{inc}}$, and $\mathcal{Z}_h(\omega) = \mathcal{R}_h(\omega) + i\mathcal{X}_h(\omega)$ is the "radiation impedance" associated with $\mathbf{j}_h$. The radiation impedances and the modes $\{\mathbf{j}_h\}$ are the eigenvalues and eigenvectors of a volume integral operator, and they do not depend on the material of the object but only on the object shape and size parameter $\xi = \omega \ell_c / c_0$. Poynting's theorem in the frequency domain, applied to the mode $\mathbf{j}_h$ in free space, relates the radiation resistance $\mathcal{R}_h$ to the average electromagnetic power radiated to infinity by the mode $\mathbf{j}_h$ and the radiation reactance $\mathcal{X}_h$ to the difference between the (time-averaged) magnetic and electric energies stored in the whole space. The radiation impedance, due to causality, satisfies the Kramers-Kronig relations.

At the frequency ω_h, when the zero-reactance condition

$$X_m(\omega_h) + \mathcal{X}_h(\omega_h) = 0$$

is met, the imaginary part of the denominator of the mode expansion of the polarization current density vanishes. Thus, the mean power scattered by the object exhibits a resonance peak near ω_h, provided that the mode $\mathbf{j}_h$ is isolated, i.e., sufficiently far in frequency from the remaining modes, and coupled with $\mathbf{E}_{\text{inc}}$. This resonance peak can then be characterized by its fractional bandwidth, namely its bandwidth divided by its center frequency. We showed that the fractional bandwidth can be determined by a formula that has the same structure as the Yaghjian-Best formula for antennas [13], but here it is associated with the material and geometrical properties of the scatterer

$$\text{FBW}_h = \frac{2}{\omega_h} \frac{R_m(\omega_h) + \mathcal{R}_h(\omega_h)}{\left|Z_m'(\omega_h) + \mathcal{Z}_h'(\omega_h)\right|}.$$

We validated the calculation of the resonance frequencies and corresponding bandwidths against the peak positions and exact bandwidths directly evaluated on the scattered power spectrum for metallic and dielectric spheres of size comparable to the resonance wavelength, finding excellent agreement.

This circuit model can be directly applied to arbitrarily shaped objects, where the radiation impedance may be evaluated by a numerical solution of the eigenvalue problem (6), as illustrated in Appendix B. It can also be extended to multiple objects made of different materials, leading to a multiport circuit model that can be investigated by using techniques borrowed from circuit theory, as shown in Appendix A.

In conclusion, the introduced circuit model rigorously captures the physics of scattering from plasmonic and dielectric nanoparticles. It can be used to directly calculate, in the full-wave regime, the resonant frequency and bandwidth of any mode supported by open resonators, independently of the excitation condition. By separating the dependencies on material characteristics from geometry, this approach allows for efficient engineering of material properties. Once the radiation impedances of the modes are determined, changes in material properties alter only the material impedance, not the radiation impedance. This characteristic makes the method particularly valuable for material dispersion engineering aimed at designing the material properties to optimize the fractional bandwidth. Furthermore, it also allows us to easily identify the scattering regimes in which radiation losses dominate over the material losses and vice versa, by comparing the resistance associated to the material impedance and the radiation resistance.

Our results facilitate the analysis, design, and optimization of nanoresonators, enabling dispersion engineering of the materials involved as a powerful tool to optimize nanophotonic circuits and passive scatterers and control their temporal dynamics, with relevant implications for the growing fields of Floquet photonics [35,36] and space-time metamaterials [37–39].

APPENDIX A: EXTENSION TO MULTIPLE MATERIALS

The proposed approach can also be extended to encompass interacting multiple objects of different materials. As an example, consider two objects, characterized by linear dimensions $\ell_c^{(1)}$ and $\ell_c^{(2)}$, with distinct but uniform susceptibilities, χ_1 and χ_2, corresponding to two material impedances $Z_m^{(1)}$ and $Z_m^{(2)}$. It is possible to define two separated auxiliary eigenvalue problems of the kind (6) for each particles, assumed to be isolated. This approach yields two sets of modes $\{\mathbf{j}_h^{(i)}\}$ and corresponding radiation impedances $\{\mathcal{Z}_h^{(i)}\}$, where the index $i = 1, 2$ labels the particle. When the two objects are coupled and excited by an external electric field $\mathbf{E}_{\text{inc}}$, the current-density field within each particle can then be approximated using N_1 modes from the first set and N_2 modes from the second set. This leads to a circuit model consisting of a $(N_1 + N_2)$ ports: N_1 of these ports are driven by a "real" voltage source, consisting of the impedance $Z_m^{(1)}$ in series with the ideal voltage source $\mathcal{E}_h^{(1)} = \langle \mathbf{j}_h^{(1)*}, \mathbf{E}_{\text{inc}} \rangle / \sqrt{\ell_c^{(1)} \langle \mathbf{j}_h^{(1)*}, \mathbf{j}_h^{(1)} \rangle}$, and the remaining N_2 ports by the series of $Z_m^{(2)}$ and $\mathcal{E}_h^{(2)} = \langle \mathbf{j}_h^{(2)*}, \mathbf{E}_{\text{inc}} \rangle / \sqrt{\ell_c^{(2)} \langle \mathbf{j}_h^{(2)*}, \mathbf{j}_h^{(2)} \rangle}$. The impedance matrix, $\mathbf{Z}$, of the multiport system is structured as a four-block matrix, with the two diagonal blocks represented by $\text{diag}\{\mathcal{Z}_1^{(1)}, \mathcal{Z}_2^{(1)}, \dots \mathcal{Z}_N^{(1)}\}$ and $\text{diag}\{\mathcal{Z}_1^{(2)}, \mathcal{Z}_2^{(2)}, \dots \mathcal{Z}_N^{(2)}\}$, and the antidiagonal blocks proportional to $\langle \mathbf{j}_h^{(i)*}, \mathscr{L}\{\mathbf{j}_k^{(j)}\} \rangle$ with $i \neq j$. The resonance frequencies and the corresponding fractional bandwidth are then determined using techniques borrowed from circuit theory.

APPENDIX B: NUMERICAL SOLUTION

The introduced circuit model can be applied to arbitrarily shaped objects by numerically solving the eigenvalue problem as defined in Eq. (6). The numerical solution requires the introduction of a volume mesh discretization of the volume V, using for instance tetrahedra or hexahedra. Following Ref. [15], we decompose the unknown current density $\mathbf{J}$ in V into its loop and star components, denoted as $\mathbf{J}_L$ and $\mathbf{J}_S$, respectively, namely $\mathbf{J} = \mathbf{J}_L + \mathbf{J}_S$, where the properties of these components are specified as

$$\nabla \cdot \mathbf{J}_L = 0 \text{ within } \mathring{V}, \quad \mathbf{J}_L \cdot \hat{\mathbf{n}} = 0 \text{ on } \partial V,$$
$$\nabla \cdot \mathbf{J}_S = 0 \text{ within } \mathring{V}, \quad \mathbf{J}_S \cdot \hat{\mathbf{n}} \neq 0 \text{ on } \partial V,$$

where $\mathring{V}$ denotes the interior of the domain V. To approximate the currents $\mathbf{J}_L$ and $\mathbf{J}_S$, we use linear combinations of loop-shape functions $\mathbf{w}_k^L$ and star-shape functions $\mathbf{w}_k^S$, respectively. The loop-shape function $\mathbf{w}_k^L$ for the k-th edge is defined by the curl of the kth edge-element shape function [55]. The star-shape functions $\mathbf{w}_k^S$, which address effects due to surface charges on the boundary ∂V, are derived similarly by taking the curl of edge-element shape functions for boundary edges. The current-density distribution is then discretized as

$$\mathbf{J} = \sum_{k=1}^{N_L} I_k^L \, \mathbf{w}_k^L + \sum_{k=1}^{N_S} I_k^S \, \mathbf{w}_k^S, \tag{B1}$$

where I_k^L and I_k^S are the degrees of freedom for the loop and star components, respectively. To derive the discrete model, we substitute the current representation from Eq. (B1) into the integral equation presented in Eq. (6). We then apply the Galerkin method, projecting the resultant expressions along both loop- and star-shape functions to ensure accurate discretization and solution approximation.

Computationally, this method is generally slower than general-purpose direct electromagnetic solvers such as the method of moments or finite difference method when calculating electromagnetic scattering for a particle or an array of particles with a specific shape and material. This is due to the computational intensity required to calculate the eigenmodes of an integral operator, as opposed to simply calculating the inverse of a matrix. Despite this, the method excels in specific scenarios. First, it provides direct insight into the positions of resonance modes and their bandwidth, which are capabilities not inherently available in direct solvers. Direct solvers require an analysis of the scattering cross-section spectra to identify peaks and associate them with modes, a process that can overlook modes unexcitable by the incident field, misinterpret peaks caused by mode interplay, and fail to clarify underlying interference phenomena. Second, this method offers significant computational advantages when addressing varying material compositions in objects of constant size and shape. Distinctly separating material properties from geometric properties, this method enables more efficient analysis. Once the radiation impedances of the modes are determined, any changes in material properties affect only the material impedance, not the radiation impedance, enhancing the method's utility in material dispersion engineering.

APPENDIX C: COMPARISON WITH PREVIOUS CIRCUIT MODELS

In this Appendix, we compare the circuit model presented in this work with the existing circuit model developed by Engheta, Salandrino, and Alù [3–5,7,8]. Their circuit model describes objects that are much smaller than the operating wavelength, and is inherently defined in the domain of electroquasistatic theory. The definition of impedances is based on *real* voltages, which are determined from an *average* potential difference, and on polarization current intensities. In contrast, our circuit model relies on a mathematical analogy rooted in the full-wave scattering theory, similar to circuit models commonly found in microwave theory. Due to these differences, as demonstrated below, our model does not return Engheta, Salandrino, and Alù's model in the low-frequency limit.

For the electric dipole mode, we compare the low-frequency limit of our circuit model, shown in Fig. 18(a), with Engheta and coworkers' circuit model, shown in Fig. 18(b). The values of the lumped elements differ between the two models. Specifically, in our model, both capacitance and inductance values are frequency independent, while in Engheta *et al.*'s model the inductance is frequency dependent. Nevertheless, both models yield the same resonance frequency. In our model the resonance frequency is

$$\omega_{\mathrm{ED}} = \frac{1}{\sqrt{L_m C_{\mathrm{ED}}^{\parallel}}} = \frac{\omega_p}{\sqrt{3}}. \tag{C1}$$

In Engheta *et al.*'s model, the resonance frequency is the solution of a second-order equation:

$$\omega_{\mathrm{ED}}^2 = \frac{1}{L_{\mathrm{sph}} C_{\mathrm{fringe}}} = \frac{\pi a \varepsilon_0 (\omega_p^2 - \omega_{\mathrm{ED}}^2)}{2\pi a \varepsilon_0} \to \omega_{\mathrm{ED}} = \frac{\omega_p}{\sqrt{3}}. \tag{C2}$$

It is useful to note that the circuit model of Ref. [3] does not allow for the calculation of the fractional bandwidth and the resonance frequency shift due to the radiation, which is possible in our model for any particle size.

APPENDIX D: LOW-FREQUENCY LIMIT PARAMETERS

First, we provide closed-form expressions for the resistance $R_h^{\parallel}$ and the inductance $L_h^{\parallel}$ of the equivalent circuit shown in Fig. 4, which describes the response of the hth plasmonic mode $\mathbf{j}_h$ in the low-frequency limit:

$$R_h^{\parallel} = \zeta_0 \frac{1}{6\pi \ell_c^3} \frac{1}{\|\mathbf{j}_h^{\parallel}\|^2} \left| \int_V \mathbf{j}_h^{\parallel}(\mathbf{r})\, d^3\mathbf{r} \right|^2 \left(\frac{\ell_c \omega}{c_0} \right)^2, \tag{D1a}$$

$$L_h^{\parallel} = -(\mu_0 \ell_c) \frac{1}{4\pi \ell_c^2} \frac{1}{\|\mathbf{j}_h^{\parallel}\|^2} \left[\oint_{\partial V} \mathbf{j}_h^{\parallel}(\mathbf{r}) \cdot \hat{\mathbf{n}}(\mathbf{r}) \oint_{\partial V} \frac{|\mathbf{r}-\mathbf{r}'|}{2} \mathbf{j}_h^{\parallel}(\mathbf{r}') \cdot \hat{\mathbf{n}}(\mathbf{r}')\, d^2\mathbf{r}' d^2\mathbf{r} + \int_V \mathbf{j}_h^{\parallel}(\mathbf{r}) \cdot \int_V \frac{\mathbf{j}_h^{\parallel}(\mathbf{r}')}{|\mathbf{r}-\mathbf{r}'|}\, d^3\mathbf{r}' d^3\mathbf{r} \right], \tag{D1b}$$

where $\mathbf{j}_h^{\parallel}$ is the electroquasistatic current modes to which the plasmonic mode $\mathbf{j}_h$ converges in the low-frequency limit, defined by the eigenvalue problem (22). These values have been obtained through the perturbative solution of the eigenvalue problem (6), following Ref. [40]. The value of $R_h^{\parallel}$ given in Eq. (D1a) vanishes when the electric dipole moment of the polarization current-density mode $\mathbf{j}_h^{\parallel}$ is zero in norm. In this case, to obtain a correct estimation of $R_h^{\parallel}$, we must consider higher-order perturbation terms in the asymptotic low-frequency limit, as shown in Ref. [40].

Next, we provide close-form expressions for the conductance $G_h^{\perp}$ and the capacitance $C_h^{\perp}$ of the equivalent circuit shown in Fig. 5, which describes the response of the hth dielectric mode $\mathbf{j}_h$ in the low-frequency limit:

$$G_h^{\perp} = \frac{1}{\zeta_0} \left(\frac{\mu_0 \ell_c}{L_h^{\perp}} \right)^2 \frac{1}{6\pi \ell_c^5} \frac{1}{\|\mathbf{j}_h^{\perp}\|^2} \left| \frac{1}{2} \int_V \mathbf{r} \times \mathbf{j}_h^{\perp}\, d^3\mathbf{r} \right|^2 \left(\frac{\ell_c \omega}{c_0} \right)^2, \tag{D2a}$$

$$C_h^{\perp} = (\varepsilon_0 \ell_c) \left(\frac{\mu_0 \ell_c}{L_h^{\perp}} \right)^2 \frac{1}{4\pi \ell_c^4} \frac{1}{\|\mathbf{j}_h^{\parallel}\|^2} \times \left[-\int_V \mathbf{j}_h^{\perp}(\mathbf{r}) \cdot \int_V \frac{|\mathbf{r}-\mathbf{r}'|}{2} \mathbf{j}_h^{\perp}(\mathbf{r}')\, d^3\mathbf{r}' d^3\mathbf{r} + \sum_{k=1}^{\infty} \frac{1}{4\pi} \frac{C_k^{\parallel}}{\varepsilon_0 \ell_c} \frac{1}{\|\mathbf{j}_k^{\parallel}\|^2} \left| \int_V \mathbf{j}_k^{\parallel}(\mathbf{r}) \cdot \int_V \frac{\mathbf{j}_h^{\perp}(\mathbf{r}')}{|\mathbf{r}-\mathbf{r}'|} d^3\mathbf{r}' d^3\mathbf{r} \right|^2 \right], \tag{D2b}$$

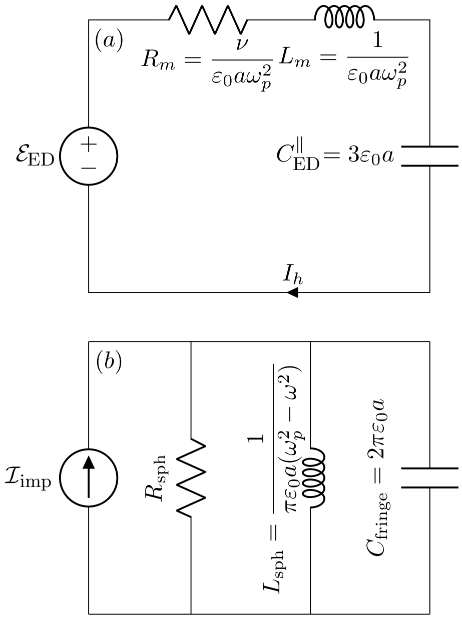

FIG. 18. Circuit models describing the response of the electric dipole mode of a Drude metal sphere (plasma frequency ω_p and damping rate ν) of radius a. (a) Electrostatic limit of the equivalent circuit model presented in this paper. (b) Equivalent circuit model introduced by Engheta, Salandrino, and Alù [3].

where $\mathbf{j}_h^{\perp}$ is the magnetoquasistatic current modes to which the dielectric mode $\mathbf{j}_h$ converges in the low-frequency limit, defined by the eigenvalue problem (24). In Eq. (D2b) the modes $\{\mathbf{j}_h^{\parallel}\}$ are the electroquasistatic current modes associated with the volume V occupied by the object. The value of $G_h^{\perp}$ given in Eq. (D2a) vanishes when the magnetic dipole moment of the polarization current-density mode $\mathbf{j}_h^{\perp}$ is zero in norm. In this case, to obtain a correct estimation of $G_h^{\perp}$, we must consider higher-order perturbation terms in the asymptotic low-frequency limit, as shown in Ref. [40].

APPENDIX E: DRUDE-LORENTZ METAL

In this section, we consider a Drude-Lorentz sphere of radius a. The Drude-Lorentz susceptibility is given by [1]

$$\chi(\omega) = -\left[\frac{\omega^2}{\omega_p^2} - i\frac{\omega\nu}{\omega_p^2} - \frac{\omega_0^2}{\omega_p^2}\right]^{-1},$$

with plasma frequency ω_p, natural frequency ω_0, damping rate ν. The material impedance, defined by Eq. (1), is

$$Z_m(\omega) = i\omega L_m + \frac{1}{i\omega C_m} + R_m \tag{E1}$$

where

$$L_m = \frac{1}{a\varepsilon_0\omega_p^2}, \quad C_m = \varepsilon_0 a\frac{1}{\eta^2}, \quad R_m = \frac{\nu}{a\varepsilon_0\omega_p^2}, \tag{E2}$$

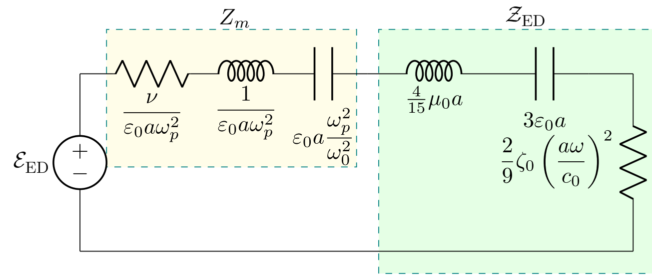

FIG. 19. Circuit model describing the low-frequency response of the electric dipole mode $\mathbf{j}_{\mathrm{ED}}$ of a Drude-Lorentz metal sphere of radius a, plasma frequency ω_p, natural frequency ω_0, and damping rate ν. Z_m is the material impedance. Z_{ED} is the radiation impedance of the electric dipole mode. The voltage $\mathcal{E}_h$ of the source is given in Eq. (13).

and

$$\eta = \frac{\omega_0}{\omega_p}. \tag{E3}$$

The circuit model of the electric dipole mode in the low-frequency limit is shown in Fig. 19. It is instructive to compare it with the corresponding circuit of a Drude metal sphere, shown in Fig. 10. As expected, the radiation impedance of the mode is unchanged since it does not depend on the material, while the material impedance exhibits an additional series capacitance. In the following, we neglect the material losses assuming $R_m \approx 0$. The resonant frequency ω_{ED} can be directly obtained from the equivalent *RLC* circuit:

$$\omega_{\mathrm{ED}} = \frac{1}{\sqrt{L_m\left(C_m \parallel C_{\mathrm{ED}}\right)}} \approx \frac{\omega_p}{\sqrt{3}}\sqrt{1+3\eta^2}, \tag{E4}$$

where

$$C_m \parallel C_{\mathrm{ED}} = \frac{3\varepsilon_0 a}{1+3\eta^2}. \tag{E5}$$

The 3-dB fractional bandwidth is given by Eq. (21):

$$\begin{aligned}\mathrm{FBW}_{\mathrm{ED}} &= \frac{2}{\omega_{\mathrm{ED}}}\frac{\left(R_m\left(\omega_{\mathrm{ED}}\right) + \mathcal{R}_{\mathrm{ED}}\left(\omega_{\mathrm{ED}}\right)\right)}{\left|Z_m'\left(\omega_{\mathrm{ED}}\right) + \mathcal{Z}_{\mathrm{ED}}'\left(\omega_{\mathrm{ED}}\right)\right|} \\ &= \frac{2}{3}\frac{1}{\left(1+3\eta^2\right)}\left(\frac{\omega_{\mathrm{ED}}}{c_0}\ell_c\right)^3.\end{aligned} \tag{E6}$$

As expected, for $\omega_0 = 0$ we obtain, as a limit case, the value of $\mathrm{FBW}_{\mathrm{ED}}$ already obtained in Eq. (39), for a Drude sphere. For $\omega_0 \neq 0$, i.e., $\eta > 0$, the bandwidth decreases as η increases.

[1] S. A. Maier, *Plasmonics: Fundamentals and Applications* (Springer, New York, USA, 2007).

[2] K. Koshelev, S. Kruk, E. Melik-Gaykazyan, J.-H. Choi, A. Bogdanov, H.-G. Park, and Y. Kivshar, Subwavelength dielectric resonators for nonlinear nanophotonics, Science **367**, 288 (2020).

[3] N. Engheta, A. Salandrino, and A. Alù, Circuit elements at optical frequencies: Nanoinductors, nanocapacitors, and nanoresistors, Phys. Rev. Lett. **95**, 095504 (2005).

[4] A. Salandrino, A. Alù, and N. Engheta, Parallel, series, and intermediate interconnections of optical nanocircuit elements. 1. Analytical solution, J. Opt. Soc. Am. B **24**, 3007 (2007).

[5] A. Alù, A. Salandrino, and N. Engheta, Parallel, series, and intermediate interconnections of optical nanocircuit elements. 2. Nanocircuit and physical interpretation, J. Opt. Soc. Am. B **24**, 3014 (2007).

[6] N. Engheta, Circuits with light at nanoscales: Optical nanocircuits inspired by metamaterials, Science **317**, 1698 (2007).

[7] Y. Sun, B. Edwards, A. Alù, and N. Engheta, Experimental realization of optical lumped nanocircuits at infrared wavelengths, Nat. Mater. **11**, 208 (2012).

[8] N. Engheta, From RF circuits to optical nanocircuits, IEEE Microw. Mag. **13**, 100 (2012).

[9] A. Alù and N. Engheta, Tuning the scattering response of optical nanoantennas with nanocircuit loads, Nat. Photonics **2**, 307 (2008).

[10] J.-J. Greffet, M. Laroche, and F. Marquier, Impedance of a nanoantenna and a single quantum emitter, Phys. Rev. Lett. **105**, 117701 (2010).

[11] A. Alù and N. Engheta, Input impedance, nanocircuit loading, and radiation tuning of optical nanoantennas, Phys. Rev. Lett. **101**, 043901 (2008).

[12] A. D. Yaghjian, Internal energy, Q-energy, Poynting's theorem, and the stress dyadic in dispersive material, IEEE Trans. Antennas Propag. **55**, 1495 (2007).

[13] A. Yaghjian and S. Best, Impedance, bandwidth, and Q of antennas, IEEE Trans. Antennas Propag. **53**, 1298 (2005).

[14] J. G. Van Bladel, *Electromagnetic Fields* (John Wiley & Sons, Hoboken, New Jersey, USA, 2007).

[15] C. Forestiere, G. Miano, G. Rubinacci, A. Tamburrino, R. Tricarico, and S. Ventre, Volume integral formulation for the calculation of material independent modes of dielectric scatterers, IEEE Trans. Antennas Propag. **66**, 2505 (2018).

[16] D. J. Bergman and D. Stroud, Theory of resonances in the electromagnetic scattering by macroscopic bodies, Phys. Rev. B **22**, 3527 (1980).

[17] C. Forestiere and G. Miano, Material-independent modes for electromagnetic scattering, Phys. Rev. B **94**, 201406 (2016).

[18] C. F. Bohren and D. R. Huffman, *Absorption and Scattering of Light by Small Particles* (John Wiley & Sons, Hoboken, New Jersey, USA, 2007).

[19] D. R. Rhodes, Observable stored energies of electromagnetic systems, J. Frank. Inst. **302**, 225 (1976).

[20] R. Fante, Quality factor of general ideal antennas, IEEE Trans. Antennas Propag. **17**, 151 (1969).

[21] C. A. Levis, A reactance theorem for antennas, Proc. IRE **45**, 1128 (1957).

[22] K. Schab, L. Jelinek, M. Capek, C. Ehrenborg, D. Tayli, G. A. E. Vandenbosch, and M. Gustafsson, Energy stored by radiating systems, IEEE Access **6**, 10553 (2018).

[23] L. J. Chu, Physical limitations of omni-directional antennas, J. Appl. Phys. **19**, 1163 (1948).

[24] H. A. Wheeler, Fundamental limitations of small antennas, Proc. IRE **35**, 1479 (1947).

[25] R. F. Harrington, Effect of antenna size on gain, bandwidth, and efficiency, J. Res. Natl. Bur. Stand., Sect. D **64D**, 1 (1960).

[26] R. Collin and S. Rothschild, Evaluation of antenna Q, IEEE Trans. Antennas Propag. **12**, 23 (1964).

[27] H. L. Thal, New radiation Q limits for spherical wire antennas, IEEE Trans. Antennas Propag. **54**, 2757 (2006).

[28] M. Gustafsson, C. Sohl, and G. Kristensson, Physical limitations on antennas of arbitrary shape, Proc. R. Soc. A: Math. Phys. Eng. **463**, 2589 (2007).

[29] M. Gustafsson, M. Cismasu, and B. L. G. Jonsson, Physical bounds and optimal currents on antennas, IEEE Trans. Antennas Propag. **60**, 2672 (2012).

[30] M. Gustafsson, D. Tayli, and M. Cismasu, *Physical bounds of antennas*, vol. TEAT-7240 of *Technical Report LUTEDX/(TEAT-7240)/1-38/(2015)*. Electromagnetic Theory Department of Electrical and Information Technology Lund University Sweden, 2015.

[31] W. Geyi, P. Jarmuszewski, and Y. Qi, The Foster reactance theorem for antennas and radiation Q, IEEE Trans. Antennas Propag. **48**, 401 (2000).

[32] W. Geyi, A method for the evaluation of small antenna Q, IEEE Trans. Antennas. Propag. **51**, 2124 (2003).

[33] G. A. E. Vandenbosch, Reactive energies, impedance, and Q factor of radiating structures, IEEE Trans. Antennas Propag. **58**, 1112 (2010).

[34] G. A. E. Vandenbosch, Simple procedure to derive lower bounds for radiation Q of electrically small devices of arbitrary topology, IEEE Trans. Antennas Propag. **59**, 2217 (2011).

[35] S. Yin, E. Galiffi, and A. Alù, Floquet metamaterials, eLight **2**, 8 (2022).

[36] E. Galiffi, R. Tirole, S. Yin, H. Li, S. Vezzoli, P. A. Huidobro, M. G. Silveirinha, R. Sapienza, A. Alù, and J. B. Pendry, Photonics of time-varying media, Adv. Photonics **4**, 014002 (2022).

[37] N. Engheta, Metamaterials with high degrees of freedom: Space, time, and more, Nanophotonics **10**, 639 (2021).

[38] C. Caloz and Z.-L. Deck-Léger, Spacetime metamaterials–Part II: Theory and applications, IEEE Trans. Antennas Propag. **68**, 1583 (2020).

[39] C. Caloz and Z.-L. Deck-Léger, Spacetime metamaterials–Part I: General concepts, IEEE Trans. Antennas Propag. **68**, 1569 (2020).

[40] C. Forestiere, G. Miano, and G. Rubinacci, Resonance frequency and radiative Q-factor of plasmonic and dieletric modes of small objects, Phys. Rev. Res. **2**, 043176 (2020).

[41] D. R. Fredkin and I. D. Mayergoyz, Resonant behavior of dielectric objects (electrostatic resonances), Phys. Rev. Lett. **91**, 253902 (2003).

[42] I. D. Mayergoyz, D. R. Fredkin, and Z. Zhang, Electrostatic (plasmon) resonances in nanoparticles, Phys. Rev. B **72**, 155412 (2005).

[43] C. Forestiere, G. Miano, G. Rubinacci, M. Pascale, A. Tamburrino, R. Tricarico, and S. Ventre, Magnetoquasistatic resonances of small dielectric objects, Phys. Rev. Res. **2**, 013158 (2020).

[44] U. Kreibig and M. Vollmer, *Optical Properties of Metal Clusters* (Springer, New York, USA, 1995).

[45] I. D. Mayergoyz, *Plasmon Resonances in Nanoparticles* (World Scientific, Singapore, 2012).

[46] M. Pascale, S. A. Mann, D. C. Tzarouchis, G. Miano, A. Alù, and C. Forestiere, Lower bounds to the Q factor of electrically small resonators through quasistatic modal expansion, IEEE Trans. Antennas Propag. **71**, 4350 (2023).

[47] A. Alù and N. Engheta, Enhanced directivity from subwavelength infrared/optical nano-antennas loaded with plasmonic materials or metamaterials, IEEE Trans. Antennas Propag. **55**, 3027 (2007).

[48] G. Colas des Francs, S. Derom, R. Vincent, A. Bouhelier, and A. Dereux, Mie plasmons: Modes volumes, quality factors, and coupling strengths (Purcell factor) to a dipolar emitter, Int. J. Opt. **2012**, 175162 (2012).

[49] M. Tribelsky, Resonant scattering of light by small particles, JETP **59**, 534 (1984).

[50] A. I. Kuznetsov, A. E. Miroshnichenko, Y. H. Fu, J. Zhang, and B. Luk'Yanchuk, Magnetic light, Sci. Rep. **2**, 492 (2012).

[51] A. I. Kuznetsov, A. E. Miroshnichenko, M. L. Brongersma, Y. S. Kivshar, and B. Luk'yanchuk, Optically resonant dielectric nanostructures, Science **354**, 846 (2016).

[52] K. Koshelev and Y. Kivshar, Dielectric resonant metaphotonics, ACS Photonics **8**, 102 (2021).

[53] A. K. Jonscher, The "universal" dielectric response, Nature **267**, 673 (1977).

[54] P. Debye, *Polar Molecules* (Dover, New York, USA, 1945).

[55] A. Bossavit, *Computational Electromagnetism: Variational Formulations, Complementarity, Edge Elements* (Academic Press, Boston, USA, 1998).